

Evolution of the Bimodal Directional Distribution of Ocean Waves*

DAVID W. WANG AND PAUL A. HWANG

Oceanography Division, Naval Research Laboratory, Stennis Space Center, Mississippi

(Manuscript received 30 August 1999, in final form 25 July 2000)

ABSTRACT

Recent results of numerical wave models have shown that the presence of a bimodal directional spreading is a robust feature at wavenumbers above the spectral peak. This directional bimodality is controlled mainly by directional transfer of energy through nonlinear wave–wave interactions. The bimodal feature has also been observed in the directional spectra derived from the spatial topography of ocean surface waves acquired by stereo-photography, image radars, and an airborne scanning lidar system. In this study, a comprehensive data analysis of the evolution of the wave directional distribution during two active wave growth periods in Lake Michigan is conducted. The wind and wave measurements are acquired by two heave–pitch–roll buoys moored at a nearshore and an offshore station. An empirical method averaging the results of the maximum likelihood method and maximum entropy method is used to estimate the directional distribution from buoy measurements. The study shows that the bimodal distribution is a distinctive and persistent feature over a broad frequency range throughout the wave growth process. The characteristics of directional bimodality are quantified by parameters related to the separation angles and the amplitudes of the sidelobes. In general, the values of the parameters are smallest near the peak frequency and increase toward both lower and higher frequencies. This frequency-dependent pattern appears to be invariant to the change of wave age throughout the wave growth process. The persistent nature of the directional bimodality indicates that the nonlinear wave–wave interaction mechanism not only actively moves wave energy away from the peak frequency into both higher and lower frequency components but also constantly redistributes wave energy into directions oblique to the wind direction. At the offshore buoy site when the wind and peak wave directions align closely, the bimodal distribution is symmetric about the wind direction. At the nearshore buoy site when the local wind and the peak wave are not moving in the same direction or the wind field is less homogeneous, the bimodal distribution is asymmetric.

1. Introduction

Until recently, wave energy directional distributions have been treated as a unimodal function. Intuitively, the wind wave energy propagates mainly in the wind direction and decreases monotonically with increasing angle to the wind. Field studies by Mitsuyasu et al. (1975), Hasselmann et al. (1980), and Donelan et al. (1985) provide parameterizations of such unimodal directional distributions with directional spreading narrowest at the peak frequency and broader toward both higher and lower frequencies. These parameterized directional distributions have been widely used for ocean wave models and engineering applications. The bimodal directional distribution, unlike the unimodal function, indicates that most wave energy is in two sidelobes

symmetrically located about the wind direction. This bimodal feature with most wave energy propagating at two directions oblique to the wind direction has been observed in studies on spatial measurements by stereo-photography and scanning radar or lidar (Phillips 1958; Cote et al. 1960; Holthuijsen 1983; Jackson et al. 1985; Wyatt 1995; Hwang et al. 2000). The directional bimodality has also been observed in temporal measurements of directional buoys and wave gauges (Brissette and Wu 1992; Young et al. 1995; Ewans 1998; Ewans and Van der Vlugt 1999). However, due to inadequate resolutions of the earlier spatial measurement instruments and controversy over the method-dependent estimations of directional distribution using temporal measurements, the directional bimodality remains an intriguing but less understood area of wind wave studies.

Numerical simulations by Banner and Young (1994) show that the presence of a bimodal directional spreading is a robust feature at wavenumbers above the spectral peak. The mechanism that maintains the bimodal feature is believed to be the directional transfer of energy through nonlinear wave–wave interactions (e.g., Hasselmann 1962; Young and Van Vledder 1993). Using directional buoy data at Maui, New Zealand, Ewans

* Naval Research Laboratory Contribution Number JA/7332—99-0044.

Corresponding author address: David Wang, Oceanography Division, Naval Research Laboratory, Stennis Space Center, MS 39529-5004.
E-mail: dwang@nrlssc.navy.mil

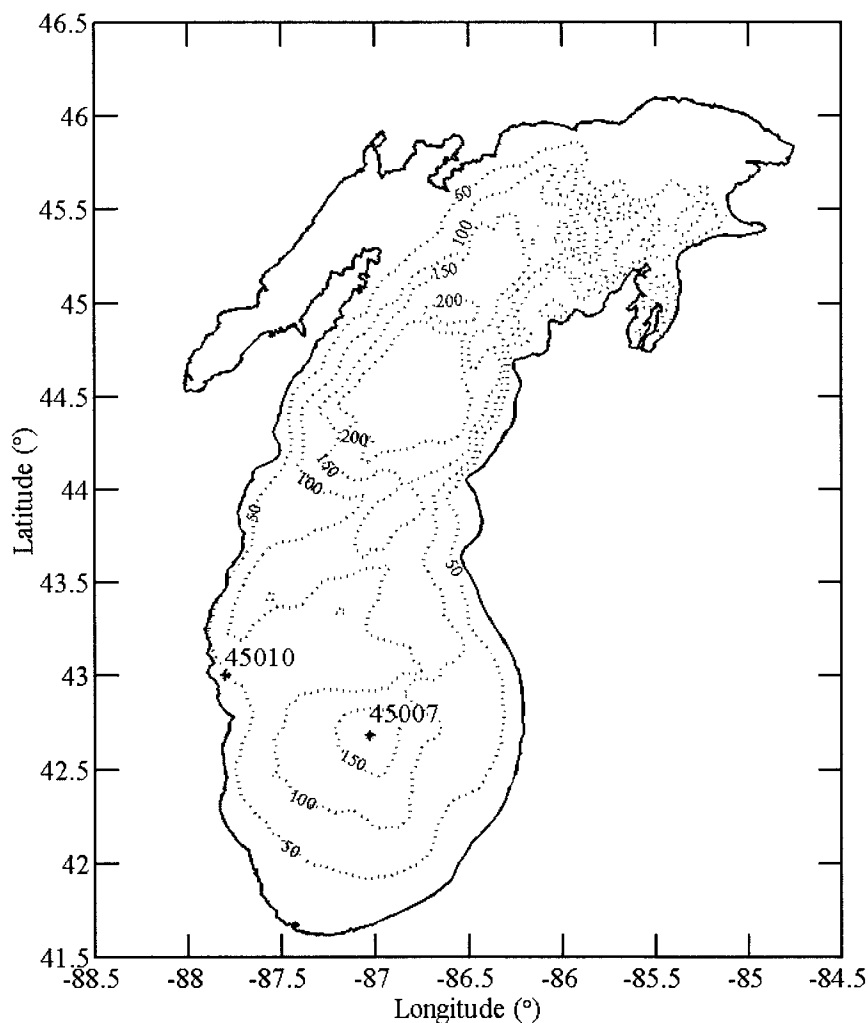


FIG. 1. Location map of the two NDBC buoy stations in southern Lake Michigan. Contour lines indicate water depths.

(1998) investigated the bimodal directional distribution of stationary wave fields under fetch-limited conditions. His results show no clear wave age dependence on the bimodal distribution parameters, which indicates that the bimodal directional distribution is an invariant property of a steady wind-generated wave field. Hwang et al. (2000) used an airborne terrain mapper (ATM, an airborne scanning laser ranging system) to acquire three-dimensional (3D) spatial topography of ocean surface waves near Duck, North Carolina. Their two-dimensional (2D) directional spectra derived from the 3D spatial measurements under a quasi-steady sea show a strong bimodal feature. The results of the ATM data agree well with model results reported by Banner and Young (1994).

In this study, we conduct data analysis on the evolution of the directional distribution during the transient periods of two wind-wave development events at two buoy stations in southern Lake Michigan. The buoy

measurement systems are described in section 2. Also presented in this section are the discussion and verification of an empirical method for estimating the directional distribution using buoy heave, pitch, and roll measurements. The marine environmental conditions and wave directional distributions during the two wave evolution events are discussed in section 3. Parameterization of directional bimodality and its dependence on frequency and wave age are examined in section 4. A summary is given in section 5.

2. Buoy measurement systems and processing methods

a. Measurement system

In this study, directional wave data are acquired from two buoy stations (ID 45007 and 45010) in Lake Michigan. Each station is deployed with a heave-pitch-roll

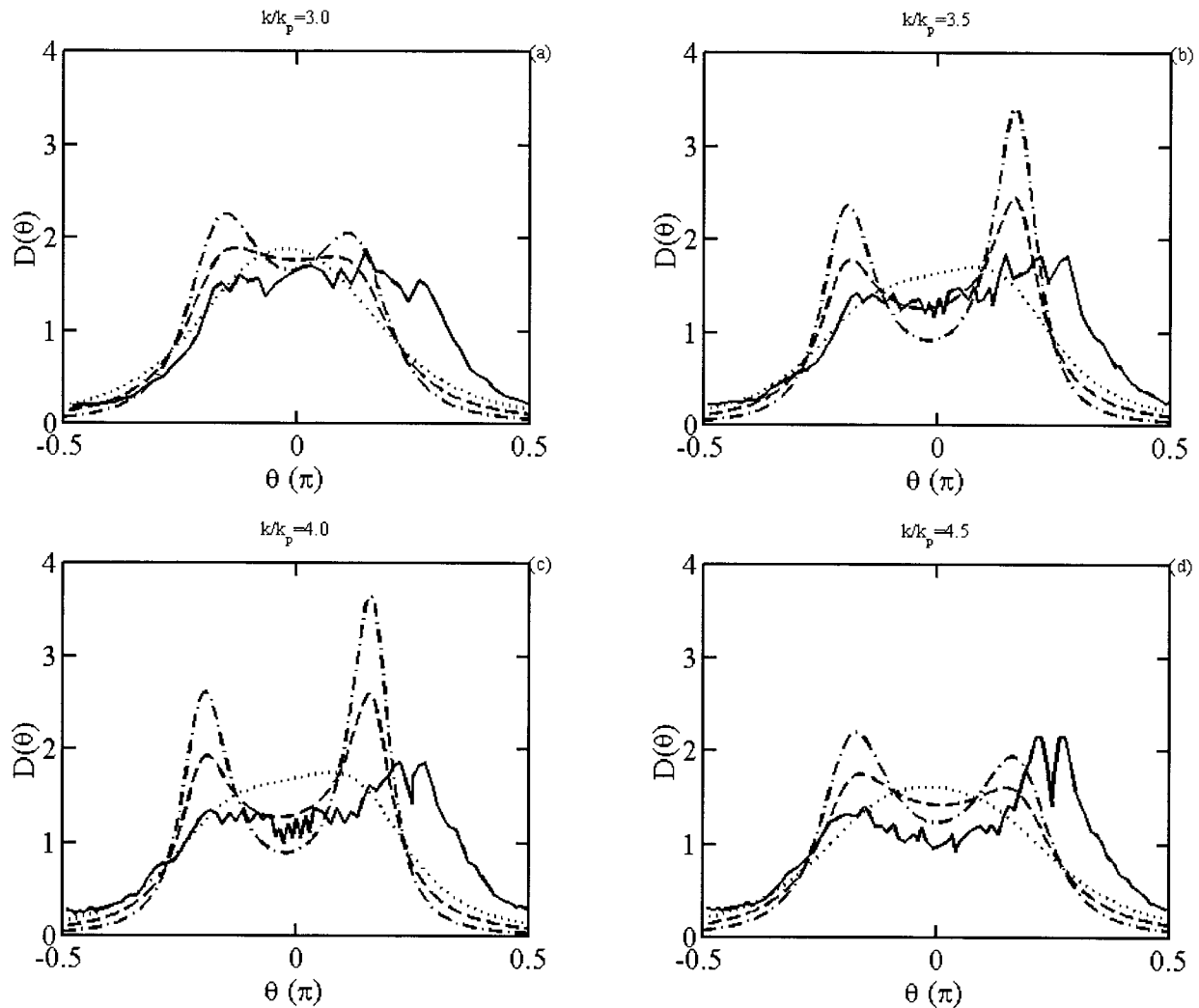


FIG. 2. Comparison of the directional distributions from the ATM measurements (solid lines) and those estimated from directional buoy measurements by the MLM (dotted lines), MEM (dashed-dotted lines), and EMP (dashed lines) at normalized wavenumbers $k/k_p = 3, 3.5, 4,$ and 4.5 . ATM and buoy data are from the Duck, North Carolina region (Hwang et al. 2000).

discus buoy maintained and operated by the National Data Buoy Center (NDBC). Buoy 45007, referred to as the offshore buoy, is moored near the center of southern Lake Michigan ($42.68^\circ\text{N}, 87.03^\circ\text{W}$), in water depth 165 m. Buoy 45010, referred to as the nearshore buoy, is moored 1.6 km offshore from Milwaukee, Wisconsin ($43.0^\circ\text{N}, 87.8^\circ\text{W}$), in water depth 15 m (Liu 1997). The location map is shown in Fig. 1. The offshore buoy is equipped with a strapped-down accelerometer measuring the buoy's heave acceleration and a triaxial magnetometer measuring the magnetic vectors for the estimation of the buoy's pitch and roll (Steele and Earle 1991) over a specified 20-min period each hour. The nearshore buoy is equipped with a Datawell Hippy 40 Mark II sensor measuring the buoy's heave, pitch, and roll over a specified 40-min period each hour. The hourly buoy motion data are processed by an onboard NDBC wave analyzer to obtain co- and quad-spectra of the

buoy's heave and the north-south and east-west slopes. Local wind speed and direction are acquired by a propeller-type wind anemometer mounted on the mast of the buoy approximately 5 m above the design waterline of the buoy hull. Average wind speed and direction, sampled over an 8-min period immediately after the buoy motion data acquisition, are computed. The hourly measured spectra and other measured meteorological and oceanographic parameters are relayed through the Geostationary Operational Environmental Satellite to NDBC for further processing and quality control. Details of the NDBC meteorological and directional wave measurement systems can be found in Steele et al. (1992) and Earle (1996). The archived co- and quad-spectra have 33 and 24 degrees of freedom (DOF), respectively, for the offshore and nearshore buoys. The difference in DOF is due to that the buoys are equipped with two different data processing systems (Earle 1996).

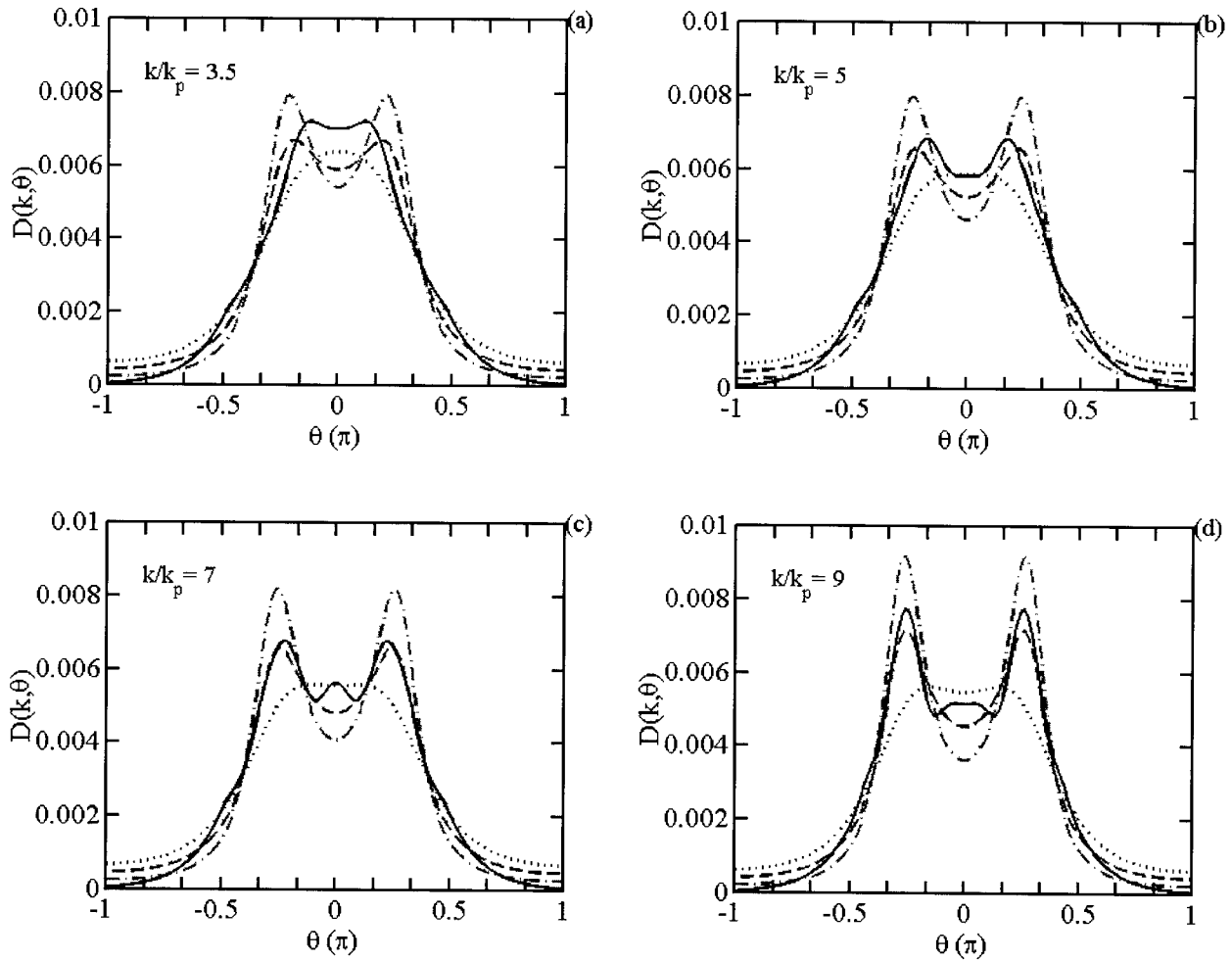


FIG. 3. Comparison of the bimodal directional distribution function $D_A(k, \theta)$ with $\beta = 0.04$ in (6) (solid lines) and the directional distributions estimated by MLM (dotted lines), MEM (dashed-dotted lines), and EMP (dashed lines) at four normalized wavenumbers $k/k_p = 3.5, 5, 7,$ and 9 .

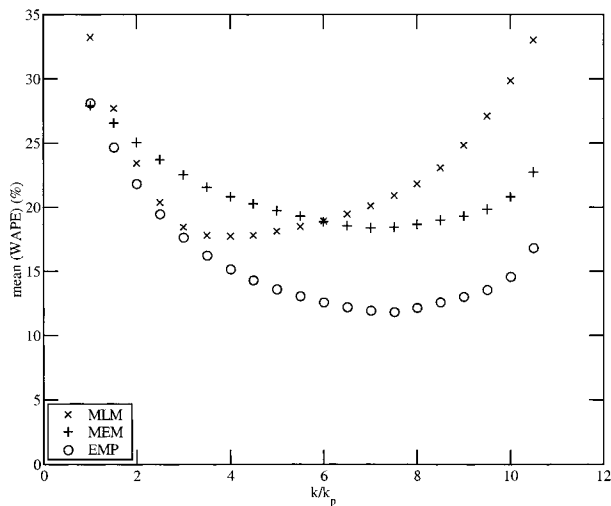


FIG. 4. Mean WAPE of five simulation comparisons ($\beta = 0.02, 0.03, 0.04, 0.05,$ and 0.06) vs normalized wavenumber for the MLM (\times), MEM ($+$), and EMP (\circ).

In this study, a three-band running average is applied to the archived spectra to further reduce data variability. This procedure increases the degrees of freedom to 99 and 72, respectively, for the offshore and nearshore buoys.

b. Processing methods for estimating the directional distribution

The 2D directional spectrum $E(f, \theta)$, which is a function of frequency f and direction θ , is often expressed as the product of the omnidirectional wave spectrum $S(f)$ and the frequency-dependent directional distribution $D(f, \theta)$,

$$E(f, \theta) = S(f)D(f, \theta), \tag{1}$$

where

$$\int_{-\pi}^{\pi} D(f, \theta) d\theta = 1. \tag{2}$$

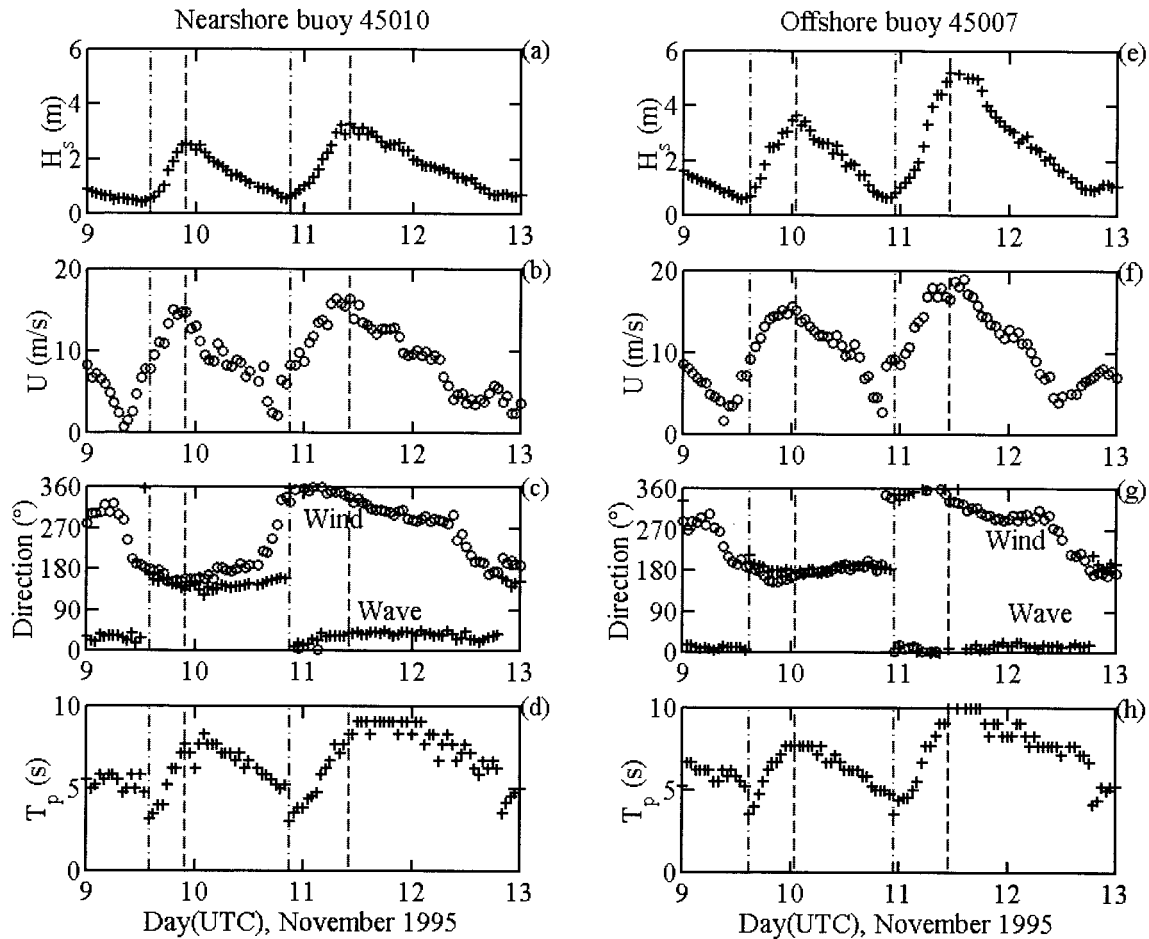


FIG. 5. Time series of hourly wind and wave measurements at the offshore buoy: (a) significant wave height H_s , (b) wind speed U , (c) wind direction θ_w (\circ) and peak wave direction θ_p ($+$), (d) peak wave period T_p ; and at the nearshore buoy: (e) significant wave height, (f) wind speed, (g) wind direction and peak wave direction, and (h) peak wave period. The vertical dashed-dotted and dashed lines, respectively, mark the beginning and the end of the two wave growth periods used.

Longuet-Higgins et al. (1963) approximate the directional distribution by Fourier series expansion,

$$D(f, \theta) = \frac{1}{2} + \sum_{n=1}^{\infty} [a_n(f) \cos n\theta + b_n(f) \sin n\theta], \quad (3)$$

where a_n and b_n are the Fourier coefficients of the n th harmonic component. The Fourier coefficients of the first two harmonic terms can be computed from the co- and quad-spectra of the buoy's heave and north-south and east-west slopes. A frequency-dependent directional parameter, referred to as the mean wave direction θ_1 , is computed from the Fourier coefficients of the first harmonic term,

$$\theta_1 = \tan^{-1}\left(\frac{b_1}{a_1}\right). \quad (4)$$

The mean wave direction θ_1 associated with the peak frequency f_p of $S(f)$ is referred to as the peak wave direction θ_p . To coincide with the established convention for wind direction measurements, NDBC reports the

wave direction as the angle from which the wave is coming, measured clockwise from true north.

In addition to the Fourier series approximation, several data-adaptive methods providing higher directional resolutions have been proposed to estimate the directional distribution from the co- and quad-spectra of buoy's heave and the north-south and east-west slopes. However, the estimated directional distributions vary significantly depending on the selected method (Benoit 1992). This method-dependent variation has caused significant disputes over the interpretation of the characteristics of the estimated directional distribution from buoy's temporal measurements, especially in cases of multimodal distributions.

As mentioned earlier, Hwang et al. (2000) present 2D directional spectral analysis on the 3D spatial topography of ocean surface waves acquired by the ATM. During the ATM data acquisition, the wind field is quasi-steady and homogenous in the region. About 50 km offshore of the ATM flight track, an NDBC buoy provides directional wave measurements. Three methods to

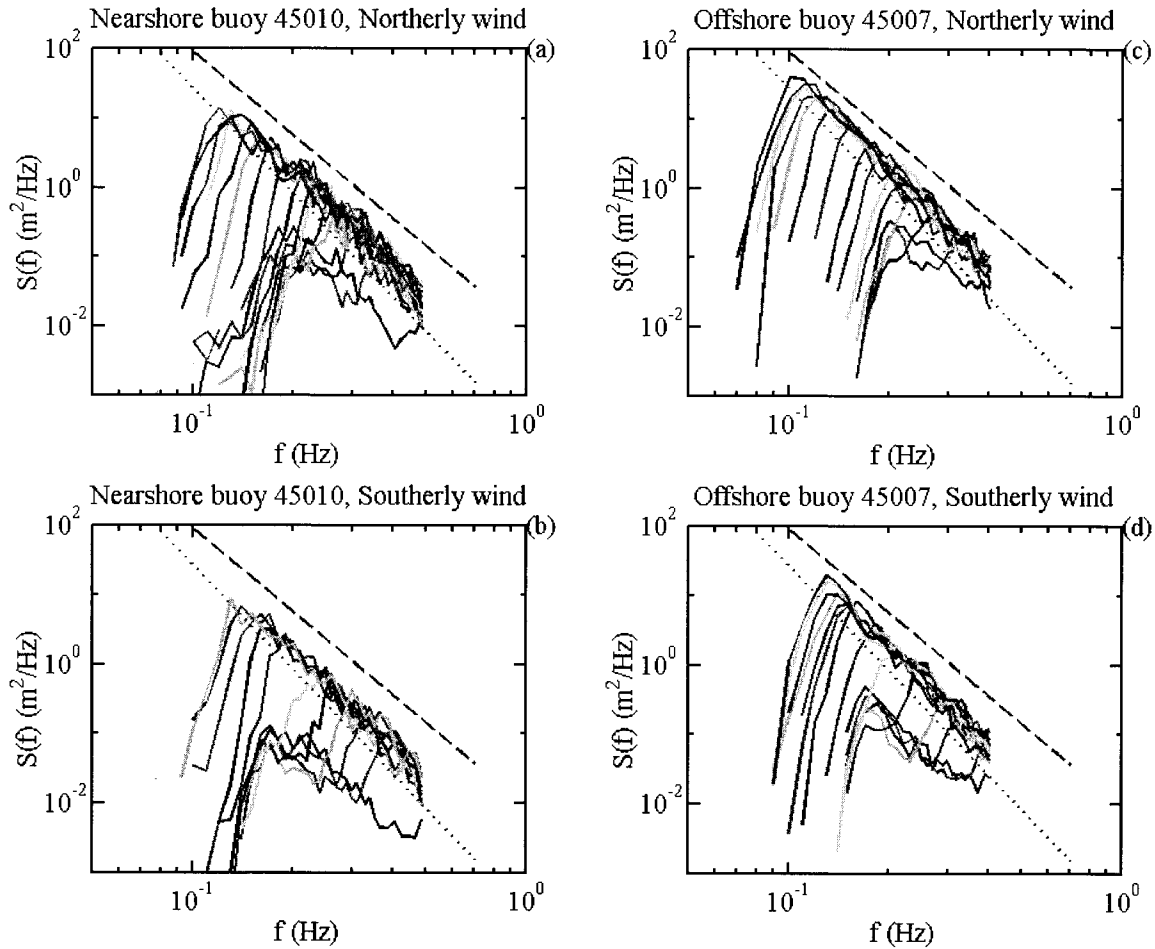


FIG. 6. The evolution of omnidirectional wave spectra at the nearshore buoy for (a) the northerly and (b) the southerly events and at the offshore buoy for (c) the northerly and (d) the southerly events. The dashed and dotted lines are the references for slopes of -4 and -5 , respectively.

estimate the directional distribution are applied to the buoy measurements. Figure 2 shows a comparison of the directional distributions from the ATM measurements and those estimated from the directional buoy measurements by the maximum likelihood method (MLM: Oltman-Shay and Guza 1984) and the maximum entropy method (MEM: Lygre and Krogstad 1986). An empirical directional distribution estimate (EMP) obtained by averaging the directional distribution estimates of the MEM and the MLM is also presented in the comparison. Directional distributions estimated by other proposed data-adaptive methods are generally between the estimates of MEM and MLM (Benoit et al. 1997). The bimodal feature of the ATM data becomes more visible at higher wavenumbers ($k > 1.3k_p$, where k is wavenumber and subscript p denotes spectral peak). The two sidelobes of the MEM estimate are much sharper and higher in amplitude than the ATM results. The MLM estimate remains broader and fails to display the bimodal feature in the wavenumber range available. The EMP estimate, by averaging the sharp and high-ampli-

tude MEM estimate with the broader MLM estimate, seems to provide a practical compromise and shows a better agreement with the ATM results. More details of the comparison are given in Hwang et al. (2000).

In order to further confirm that the EMP provides a better estimate of directional distribution than the MLM and MEM, we conduct a numerical simulation test similar to the ones reported in several other studies (Lygre and Krogstad 1986; Brissette and Tsanis 1994; Young 1994). In such tests, the co- and quad-spectra of the wave elevation, north-south and east-west slopes are simulated from a predefined target directional distribution function. The first four Fourier coefficients of the Fourier series expansion of $D(f, \theta)$ in (3) can be computed from the spectra. The MLM, MEM, and EMP then use these Fourier coefficients to estimate the directional distribution. The comparisons are made between the predefined target and the estimated directional distribution functions by the three methods. In the present simulation test, the target distribution function is the bimodal directional distribution derived from the 2D

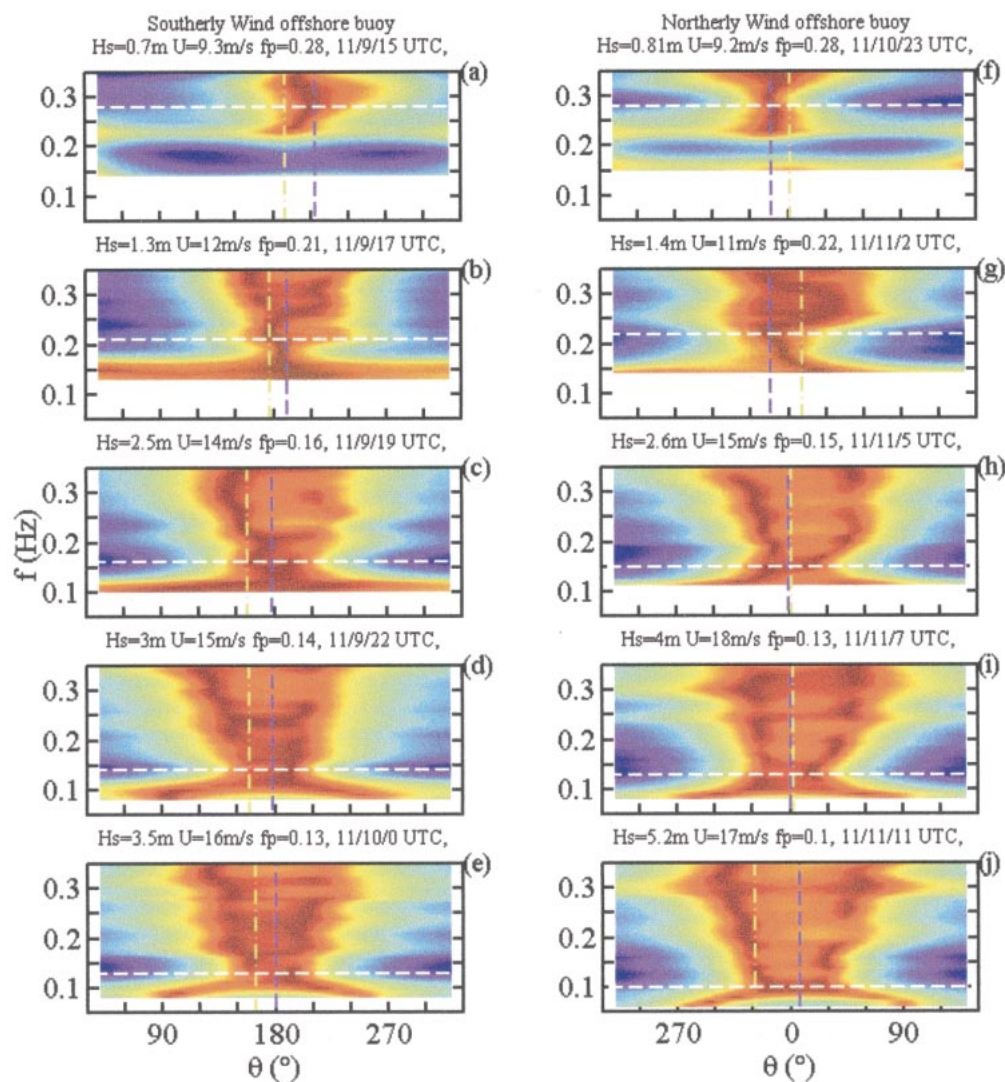


FIG. 7. Color-shaded image of the 2D directional distributions at the offshore buoy. The directional distributions are from the 1st, 3rd, 5th, 7th, and the last hours of the southerly event (a–e) and from the 1st, 4th, 7th, 9th and the last hours of the northerly event (f–j). The peak wave frequencies are indicated by the horizontal white dashed lines. The wind and peak wave directions are marked as yellow dashed–dotted and blue dashed lines, respectively. The directional distribution is normalized by the maximum value at each frequency and displayed in logarithmic scale. Darker red color corresponds to higher level of the normalized distribution density.

spectral analysis of the 3D spatial topography of quasi-steady ocean surface waves acquired by ATM (Hwang et al. 2000). The directional function at each wave-number is Fourier decomposed into nine terms,

$$D_1(k, \theta) = \frac{1}{\pi} \left[1 + \sum_{n=1}^9 2A_n(k) \cos 2n\theta \right], \quad -\pi/2 \leq \theta \leq \pi/2. \quad (5)$$

[It is noted that the factor 2 in the Fourier coefficients is missing in Eqs. (7) and (8) in Hwang et al (2000).] Each of the nine Fourier components, $A_n(k)$, is fitted by a least squares third-order polynomial, the coefficients of which are tabulated in Table 1 of Hwang et al. (2000).

Because $D_1(k, \theta)$ only covers the range from $-\pi/2$ to $\pi/2$, an expansion to $-\pi$ and π is made by adding an exponentially decreasing curve at both ends of $D_1(k, \theta)$. The expansion curve can be expressed as

$$D_2(k, \theta) = 0.5D_1(k, \pi/2) \exp(-\beta|\theta_*|), \quad (6)$$

where $\theta_* = |\theta| - \pi/2$ and β is an empirical constant; $D_2(k, \theta)$ has its maximum value at $\theta = \pm\pi/2$ and decreases as θ moves away from $\pm\pi/2$. A larger value of β results in a shaper decrease of the expansion curve, which means a narrower directional spreading. To correct the edge effect of directional aliasing in $D_1(k, \theta)$ caused by 180° folding of the 2D image processing, $D_2(k, \theta)$ is subtracted from $D_1(k, \theta)$ in the range of $-\pi/2$

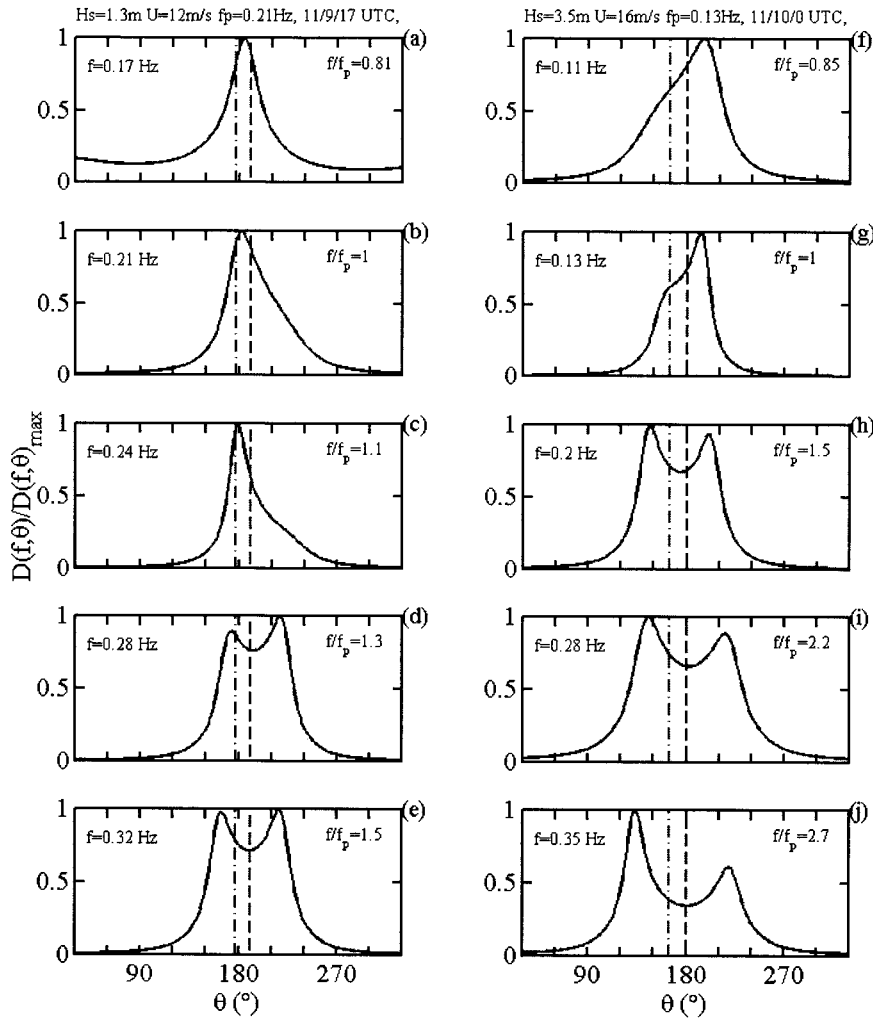


FIG. 8. Frequency slices from the 2D directional distribution of the 3d hour of the southerly event (Fig. 7b) at frequencies of 0.17, 0.21, 0.24, 0.28, and 0.32 Hz, (a–e) and from the 2D directional distribution of the last hour of the southerly event (Fig. 7e) at frequencies of 0.11, 0.13, 0.2, 0.28, and 0.35 Hz (f–j). The wind and peak wave directions are marked as dashed–dotted and dashed lines, respectively.

$\leq \theta \leq \pi/2$. The target directional distribution function of ATM is then expressed as

$$D_A(f, \theta) = \frac{D_M(f, \theta)}{\int_{-\pi}^{\pi} D_M(f, \theta) d\theta}, \quad -\pi \leq \theta \leq \pi, \quad (7)$$

where

$$D_M(k, \theta) = \begin{cases} D_1(k, \theta) - D_2(k, \theta), & -\pi/2 \leq \theta \leq \pi/2 \\ D_2(k, \theta), & \pi/2 \leq |\theta| \leq \pi. \end{cases} \quad (8)$$

Figure 3 shows $D_A(k, \theta)$ (solid lines) at $k/k_p = 3.5, 5, 7,$ and 9 with $\beta = 0.04$ in (6). Also shown are three estimated distribution functions, $D_E(k, \theta)$, by the MLM (dotted lines), MEM (dashed–dotted lines), and EMP (dashed lines). The $D_A(k, \theta)$ shows a bimodal distri-

bution. The MEM estimate has much sharper and higher peaks than $D_A(k, \theta)$ at the same wavenumbers. The MLM estimate remains broader than $D_A(k, \theta)$ and fails to show the bimodal feature. The EMP estimate gives a better agreement with the $D_A(k, \theta)$ by averaging the estimates of MLM and MEM. These findings are consistent with the results of the field data comparison given in Hwang et al. (2000). Differences between $D_A(k, \theta)$ and $D_E(k, \theta)$ by the three methods at a given wavenumber k can be quantified by the weighted average percent error (WAPE) denoted by ε (Oltman-Shay and Guza 1984),

$$\varepsilon = \frac{\sum_{\theta} |D_E(k, \theta) - D_A(k, \theta)|}{\sum_{\theta} D_A(k, \theta)} \times 100, \quad -\pi \leq \theta \leq \pi. \quad (9)$$

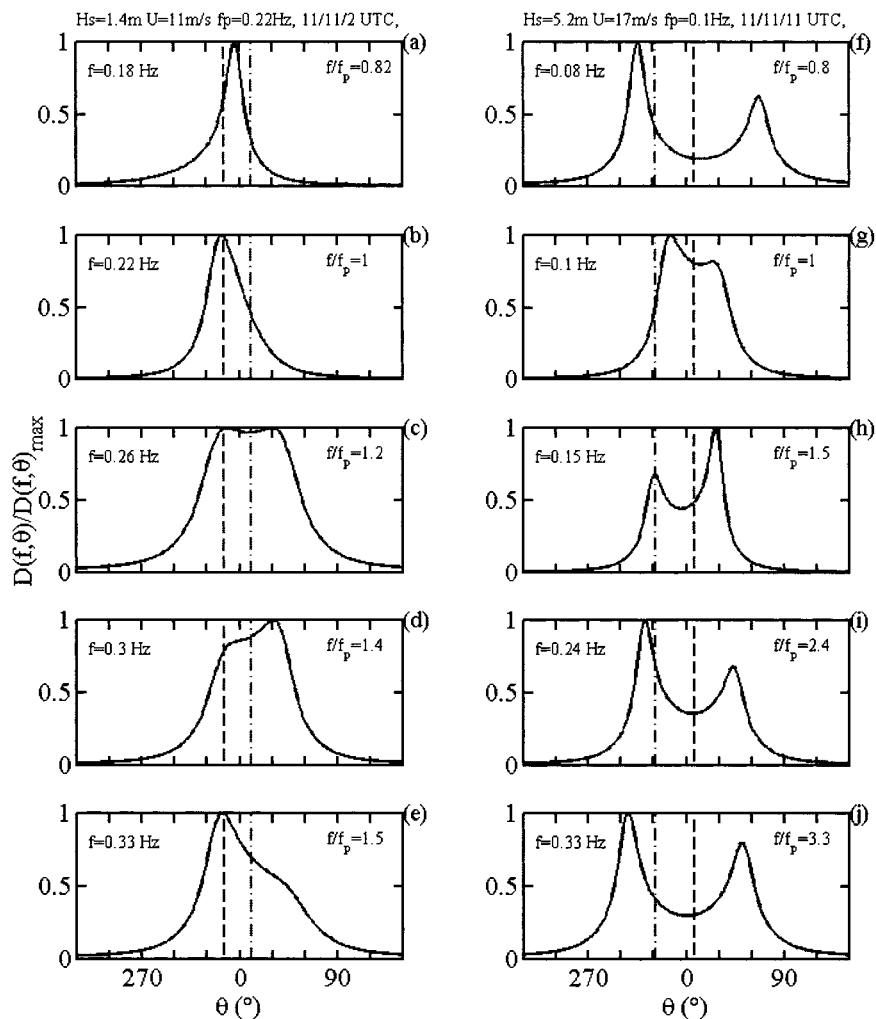


FIG. 9. Frequency slices from the 2D directional distribution of the 4th hour of the northerly event (Fig. 7g) at frequencies of 0.18, 0.22, 0.26, 0.30, and 0.33 Hz (a–e) and from the 2D directional distribution of the last hour of the northerly event (Fig. 7j) at frequencies of 0.08, 0.1, 0.15, 0.24, and 0.33 Hz (f–j). The wind and peak wave directions are marked as dashed-dotted and dashed lines, respectively.

The simulation test is also carried out for $\beta = 0.02, 0.03, 0.05,$ and 0.06 to further compare the three methods under various spreading widths of $D_A(k, \theta)$. Figure 4 shows the mean WAPE of the five simulation comparisons ($\beta = 0.02, 0.03, 0.04, 0.05,$ and 0.06) versus the normalized wavenumber k/k_p . The values of the mean and standard deviation of WAPE of the five simulation comparisons at different k/k_p are also tabulated in Table 1. The EMP provides the closest fit to $D_A(k, \theta)$ with its mean WAPE less than those of the MLM and MEM, especially at higher wavenumbers where the bimodal distribution is significant. The standard deviations of WAPE of the MEM are much higher than those of the MLM and EMP. This larger variance is due to the high numerical variability of the MEM as reported by Lygre and Krogstad (1986). The mean WAPE of the MLM are very close to those of the EMP at $k/k_p < 4$,

but the MLM fails to show the bimodality in the target distribution (Figs. 2b and 3a). As the bimodal feature becomes more significant at higher wavenumbers, the mean WAPE of the MLM is larger than those of the MEM and EMP. This simulation comparison confirms that the EMP, by averaging the estimates of the MLM and MEM, provides a better estimate of directional distribution from buoy measurements. In the following analysis, the directional distribution is estimated by the EMP.

3. Results

a. Environmental conditions

Figure 5 shows the time history of hourly wind and wave data (wind speed U , wind direction θ_w , significant

wave height H_s , peak wave period T_p , and peak wave direction θ_p) from 9 to 13 November 1995 at the offshore and nearshore buoys. The winds and waves at the nearshore buoy follow closely with those at the offshore buoy. This suggests relatively homogeneous wind and wave fields in the area. Two strong wind events occur. The predominant wind of the first event is southerly. About one and a half days later, the wind shifts to predominantly northerly during the second event. Each event starts with a rapid increase of wind speed and wave height, while the wind direction remains relatively steady. At the end of the rapid wave growth, the wave field remains quasi-steady for a few hours. The event is then followed by a long period of wave decay. The wave growth periods of the first and the second events are referred to as the southerly and the northerly events, respectively. Vertical dashed-dotted and dashed lines in Fig. 5, respectively, mark the beginning and the end of the wave growth periods of the two events. The northerly event has a much longer fetch for wind wave development at both buoy locations than that of the southerly event. This is due to the geometry of Lake Michigan with the long axis aligned in the north-south direction. Wind and wave statistics are summarized in Table 2 and will be further discussed later.

Figure 6 shows the evolution of hourly omnidirectional wave spectra of the southerly and northerly events at the two buoy locations. For reference, the slopes of the dashed and dotted lines shown in the figures are -4 and -5 , respectively. The wind-generated wave energy starts to appear at the high frequency end at the beginning of wave growth and then gradually moves into the lower frequency region as waves continue to grow. The spectral slopes in the frequency region above peak frequency fall between -4 and -5 throughout the evolution. These features are consistent with other observations of wave growth (e.g., Donelan et al. 1985; Phillips 1985).

b. Evolution of the directional distribution at the offshore buoy

During the southerly event, the wind speed increases from 9.3 to 15.7 m s^{-1} as the wind-generated significant wave height reaches 3.64 m with a peak period of 7.7 s . The wave age, defined as the ratio of the phase velocity at peak period to the wind speed component in the peak wave direction, varies from 0.60 to 0.87 . Later on, during the northerly event, the wind speed increases from 9.2 to 18 m s^{-1} . The significant wave height at the end of the northerly event reaches 5.2 m with a peak wave period of 10 s . The wave age varies from 0.63 to 1.15 . The average wind directions of the southerly and northerly events are 168° and 2° , respectively, which are slightly different from the 186° and 350° average peak wave directions for the two events (Fig. 5g). The differences between the average wind and peak wave directions of the two events are considered to be insignificant,

given the 10° NDBC stated system accuracy for wind direction (Gilhousen 1987) and the sampling variability associated with the directional wave data (Krogstad 1990).

Figure 7 shows the color-shaded images of the 2D directional distributions of five different hours of the southerly (Figs. 7a-e) and the northerly events (Figs. 7f-j). The wind direction, θ_w , and the peak wave direction, θ_p , are marked as the vertical yellow dashed-dotted and blue dashed lines, respectively. To further illustrate details of the directional distribution, frequency slices extracted from the 2D directional distributions near the beginning and end of the southerly and northerly events are plotted in Figs. 8 and 9, respectively.

The color-shaded 2D images in Fig. 7 show that the directional spreading is narrowest at f_p and broadens as frequency moves toward higher or lower frequency regions. The directional distribution is approximately symmetric with respect to θ_w and θ_p . At the beginning of wave growth, most wave energy concentrates at higher frequencies and propagates in the wind direction. No significant bimodal distribution is visible (Figs. 7a,g; 8a-c,f,g; and 9a,b) in the range measured. It is possible that the bimodal distribution is present at frequencies higher than 0.35 Hz , which is the upper frequency limit of the wave measurement system at the offshore buoy. As waves continue to grow, the wave energy no longer concentrates around θ_w and θ_p . Instead, most wave energy is at two sidelobes more or less symmetrically located on both sides of θ_p (Figs. 7d,e,i,j; 8d,e,h-j; and 9h-j). The angular separation distance between the two sidelobe peaks is smallest near f_p and increases as the wave frequency moves away from f_p .

c. Evolution of directional distributions at the nearshore buoy

Under similar wind conditions as those at the offshore buoy, the significant wave height during the southerly event at the nearshore buoy increases from about 0.5 to 2.52 m with a peak period of 7.7 s . The wave age varies from 0.58 to 0.75 . During the northerly event, the significant wave height reaches 3.28 m with a peak period of 8.3 s . The wave age varies from 0.58 to 1.12 . The average peak wave direction of the northerly event is 33° , which is 42° more northeasterly than the average wind direction of 351° . The difference between wind and peak wave directions under a quasi-steady wind may be attributed to the slant fetch effect (Donelan et al. 1985; Gilhousen 1989; Walsh et al. 1989), which occurs when the offshore wind blows at an oblique angle to the shoreline orientation producing an asymmetric fetch with respect to the wind direction. As a result, instead of following the wind direction, the waves are primarily from the direction of longer fetch (i.e., the offshore side when following the wind direction). The slant fetch effect also causes the difference between the wind and peak wave directions for the southerly event (Fig. 5c).

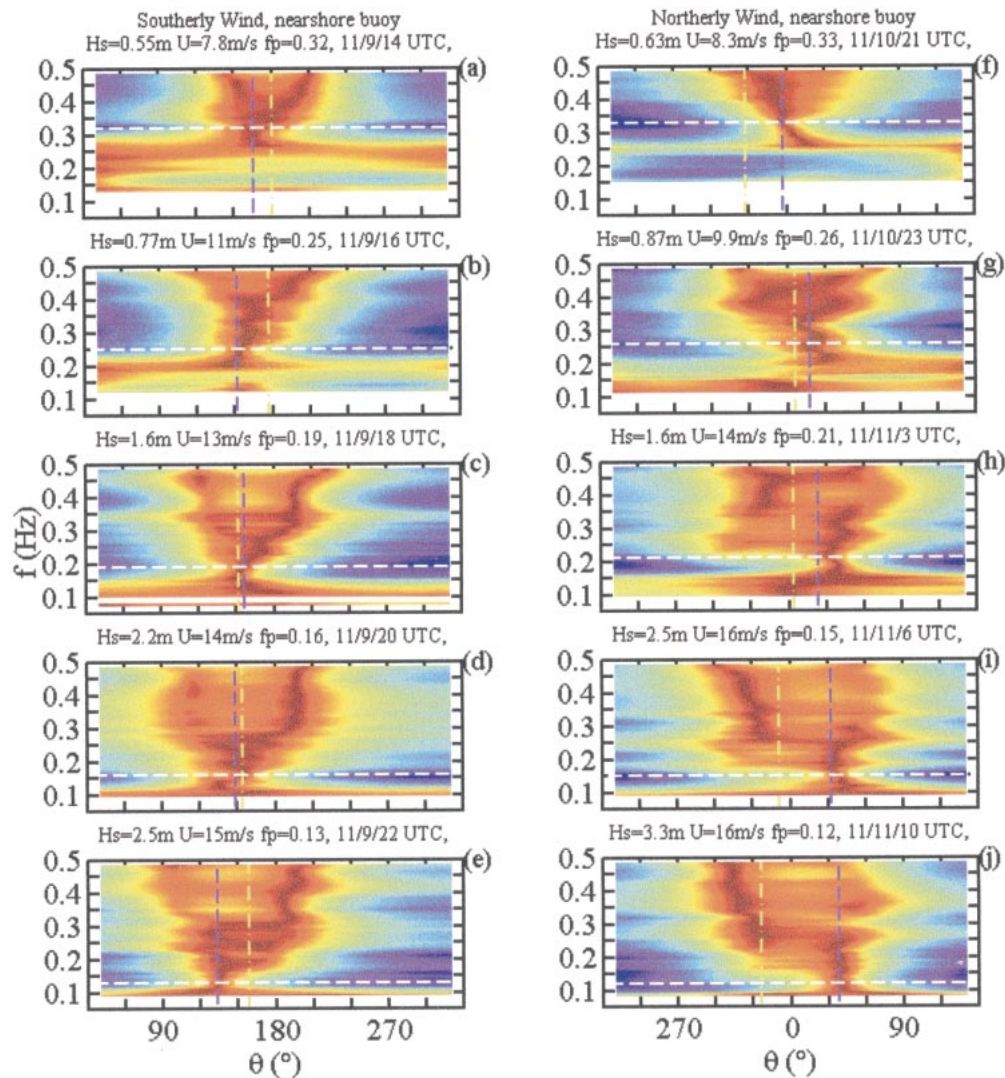


FIG. 10. Color-shaded image of the 2D directional distributions at the nearshore buoy. The directional distributions are from the 1st, 3rd, 5th, 7th, and the last hours of the southerly event (a–e) and from the 1st, 4th, 7th, 10th, and the last hours of the northerly event. (f–j) The line styles and color image scales are the same as those in Fig. 7.

The difference is less pronounced due to the wind fetch for the southerly wind being shorter than that for the northerly wind.

Figure 10 shows the color-shaded images of the 2D directional distributions at five different hours of the southerly (Figs. 10a–e) and the northerly events (Figs. 10f–j). Frequency slices extracted from the 2D directional distributions near the beginning and the end of the wave growth periods are shown in Figs. 11 and 12 for the southerly and northerly events, respectively. The wave measurement system installed on the nearshore buoy provides directional distributions up to 0.485 Hz, which is significantly higher than the 0.35-Hz upper frequency limit at the offshore buoy.

The directional spreading is narrowest at the peak frequency and broadens as the frequency moves away

from peak frequency into either higher or lower frequency region. At the beginning of the two events, the wave energy concentrates around the wind direction. Bimodal distribution is visible at very high frequencies (Figs. 10a,f; 11a–e; and 12a–e). As wind and wave continue to grow, the bimodal distribution becomes more evident in most frequencies (Figs. 10d,e,i,j; 11f–j; and 12f–j). These findings are very similar to those observed at the offshore buoy.

Near the end of the northerly event, the wind shifts to a more northwesterly direction as the peak wave direction shifts to a more northeasterly direction. The difference of wind and peak wave directions reaches 60° at the end of the northerly event. As the difference between wind and wave directions gradually increases, the bimodal directional distribution becomes more asym-

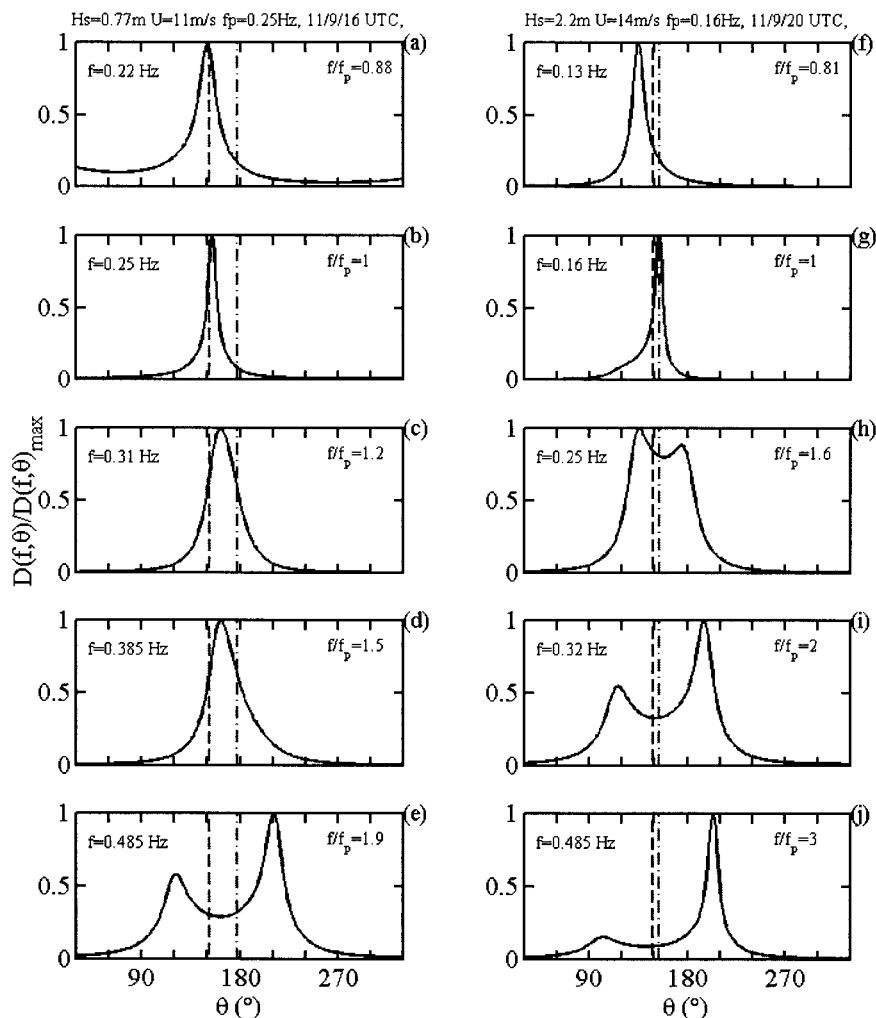


FIG. 11. Frequency slices from the 2D directional distribution of the 3d hour of the southerly event (Fig. 10b) at frequencies of 0.22, 0.25, 0.31, 0.385, and 0.485 Hz (a–e) and from the 2D directional distribution of the 7th hour of the southerly event (Fig. 10d) at frequencies of 0.13, 0.16, 0.25, 0.32, and 0.485 Hz (f–j). The wind and peak wave directions are marked as dashed-dotted and dashed lines, respectively.

metric (Figs. 10h–j). The asymmetric bimodal distributions at higher frequencies (Figs. 12i–j) show that the amplitude of the sidelobe closer to the wind direction is significantly higher than that of the sidelobe closer to the peak wave direction. The directional distributions near the peak frequency (Figs. 12g and 12h) show an asymmetric unimodal distribution with the maximum amplitude at the peak wave direction. The strong asymmetry in the directional distributions of the northerly event is apparently related to the larger difference between wind and peak wave directions and also the less homogeneous wind field as a result of land proximity. Similar asymmetric features are found in the southerly event, although the difference between wind and peak wave directions is relatively small. The larger asymmetry at higher wave frequencies may reflect the effect

of small-scale wind direction fluctuation. This point will be further studied in the near future.

4. Discussions

a. Definition of bimodal parameters

To quantify the characteristics of the directional bimodality, parameters related to the angular locations and the amplitudes of the sidelobes are defined in Fig. 13. The direction is defined based on their respective locations in the coordinate system shown, the lobe on the left-hand side when following the wind direction is referred to as Lobe₁ and the other lobe is referred to as Lobe₂. As the wind direction is generally at the center of the bimodal directional distribution, for the southerly

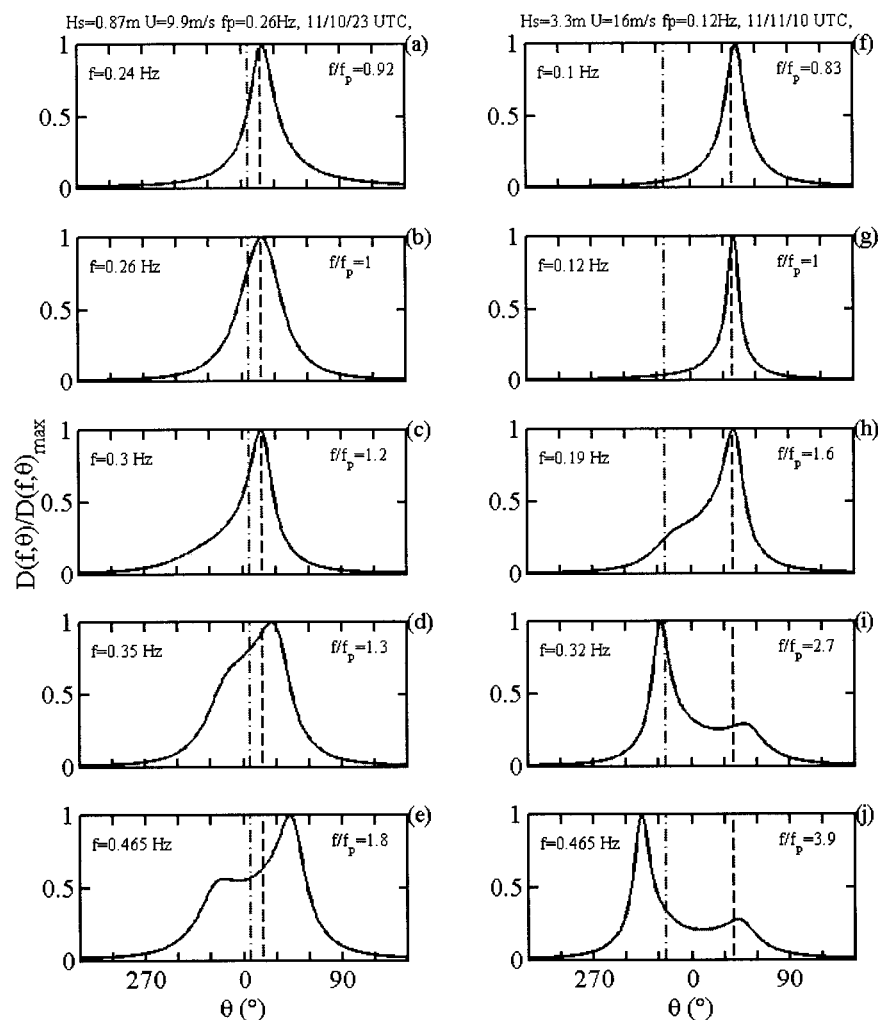


FIG. 12. Frequency slices from the 2D directional distribution of the 3d hour of the northerly event (Fig. 10g) at frequencies of 0.24, 0.26, 0.3, 0.35, and 0.465 Hz (a–e) and from the 2D directional distribution of the last hour of the northerly event (Fig. 10j) at frequencies of 0.1, 0.12, 0.19, 0.32, and 0.465 Hz (f–j). The wind and peak wave directions are marked as dashed–dotted and dashed lines, respectively.

wind event, Lobe₁ is at a more southeasterly direction and Lobe₂ is at a more southwesterly direction. Likewise, for the northerly wind event, Lobe₁ is at a more northwesterly direction and Lobe₂ is at a more northeasterly direction.

The peaks of Lobe₁ and Lobe₂ are at directions α_1 and α_2 , respectively. The lowest point between the two lobe peaks is at direction α_0 . The lobe angles θ_{Lobe1} and θ_{Lobe2} are defined as the angular separation distances from α_1 and α_2 to α_0 , respectively. The ratios $D(f, \alpha_1)/D(f, \alpha_0)$ and $D(f, \alpha_2)/D(f, \alpha_0)$ are referred to as r_{Lobe1} and r_{Lobe2} , respectively. The lobe ratio r_{Lobe} is the average of r_{Lobe1} and r_{Lobe2} ,

$$r_{\text{Lobe}} = \frac{r_{\text{Lobe1}} + r_{\text{Lobe2}}}{2}, \quad (10)$$

and the lobe separation angle θ_{Lobe} is the average of θ_{Lobe1} and θ_{Lobe2} ,

$$\theta_{\text{Lobe}} = \frac{\theta_{\text{Lobe1}} + \theta_{\text{Lobe2}}}{2}. \quad (11)$$

b. Lobe separation angle

As observed in the directional distributions of the northerly and southerly events, the directional bimodality is a distinctive and persistent feature throughout the wave growth period. Figure 14a shows the lobe separation angle θ_{Lobe} as a function of the normalized frequency f/f_p at five different hours of the northerly event at the offshore buoy. During the period, the significant wave height increases from 1.66 to 5.2 m and

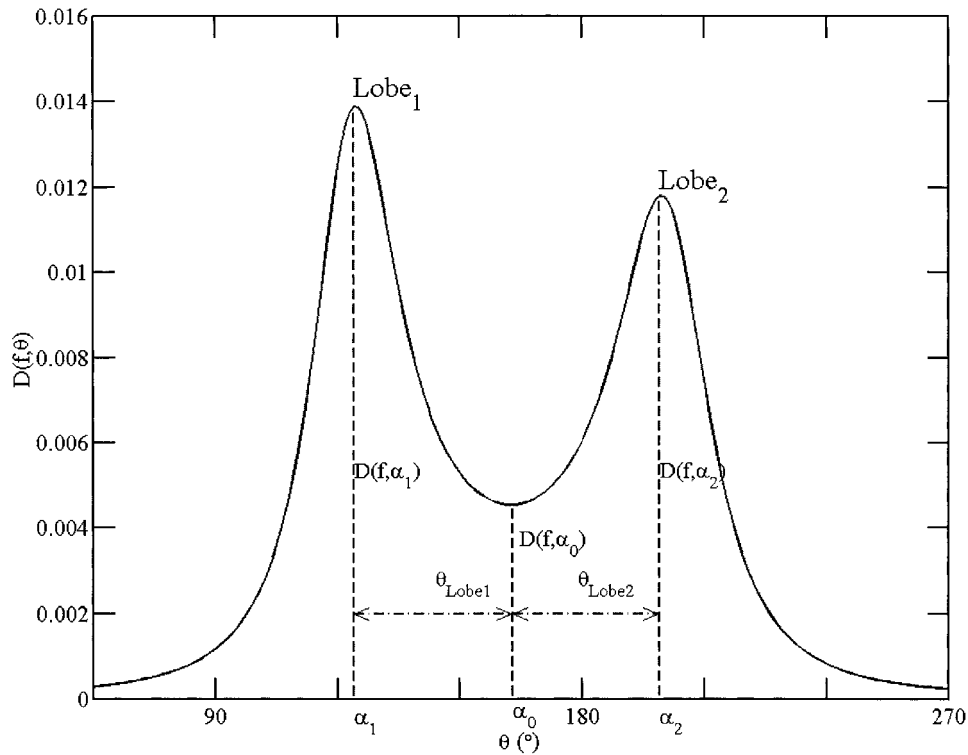


FIG. 13. Definition sketch of the parameters used to characterize the bimodal distribution.

the wave age varies from 0.63 to 1.15. In spite of significant data scatter, there is a general trend that θ_{Lobe} increase as the frequency moves away from $f/f_p = 1$. No evidence indicates a systematic variation of θ_{Lobe} at a given f/f_p with respect to the change of wave ages, although a weak dependence on the wave age may not be excluded due to data scatter. This is further confirmed in plots of the lobe separation angle θ_{Lobe} versus the wave age for a given range of f/f_p (not shown). Similar results are also found in the lobe separation angles for the southerly event at the offshore buoy and for the southerly and northerly events at the nearshore buoy.

Because the dependence of θ_{Lobe} on f/f_p is invariant to the wave age during the wave growth events, the θ_{Lobe} of each event are then grouped into f/f_p bins with a 0.2 f/f_p bin width. Figure 15 shows the bin-averaged lobe separation angle, $\langle \theta_{\text{Lobe}} \rangle$, versus f/f_p for the two events at the nearshore and offshore buoys. The dashed curves represent the calculated results of a nonlinear wave-wave interaction model (Plate 1 of Young et al. 1995; Fig. 11 of Ewans 1998). The dashed-dotted curves in the range $1.3 < f/f_p < 2.65$ represent the ATM results (Hwang et al. 2000). The two dotted curves at $f/f_p > 1$ are, respectively, the upper and lower bounds of the results of the Maui buoy data reported by Ewans (1998). At $f/f_p > 1$, all four curves show that lobe separation angle increases with increasing frequency. At $f/f_p < 1$, the model curve shows that lobe separation angle increases rapidly and linearly as frequency decreases from

the peak frequency. For the northerly and southerly events at the offshore buoy, $\langle \theta_{\text{Lobe}} \rangle$ has its smallest value of about 20° at $f/f_p = 1$ and increases toward both higher and lower frequencies (Figs. 15c and 15d). $f/f_p < 1$, the trend of increasing $\langle \theta_{\text{Lobe}} \rangle$ is consistent with the model results. At $f/f_p > 1$, $\langle \theta_{\text{Lobe}} \rangle$ is between the upper and lower bounds of the Ewans results. In the range $1 \leq f/f_p \leq 2$, $\langle \theta_{\text{Lobe}} \rangle$ is closer to the upper bound curve and higher than the model and ATM curves. As frequency moves closer to $f/f_p = 2.2$, the $\langle \theta_{\text{Lobe}} \rangle$, model, and ATM curves gradually converge to the middle of the upper and lower bounds of the Ewans results. For the southerly events at the nearshore buoy (Figs. 15b), $\langle \theta_{\text{Lobe}} \rangle$ shows a similar dependence on f/f_p as those at the offshore buoy (Figs. 15c and 15d). At $f/f_p \leq 2$, $\langle \theta_{\text{Lobe}} \rangle$ is slightly above the model curve and becomes slightly lower than the model curve at $f/f_p > 2$. For the northerly event at the nearshore buoy (Figs. 15a), the dependence of $\langle \theta_{\text{Lobe}} \rangle$ on f/f_p is weaker than those at the offshore buoy (Figs. 15c and 15d). In the range $1 < f/f_p < 3$, $\langle \theta_{\text{Lobe}} \rangle$ has a small value of about 35° at $f/f_p = 1.5$ and increases to about 40° as frequency increases to $f/f_p > 3$. The trend of increasing $\langle \theta_{\text{Lobe}} \rangle$ is similar to the other cases. There is a slightly larger standard deviation in each f/f_p bin at the nearshore buoy (Figs. 15a and 15b) than those at the offshore buoy (Figs. 15c and 15d). Causes for the larger variations include lower DOF (72 for the nearshore buoy versus 99 for the offshore buoy), less homogeneous wind field

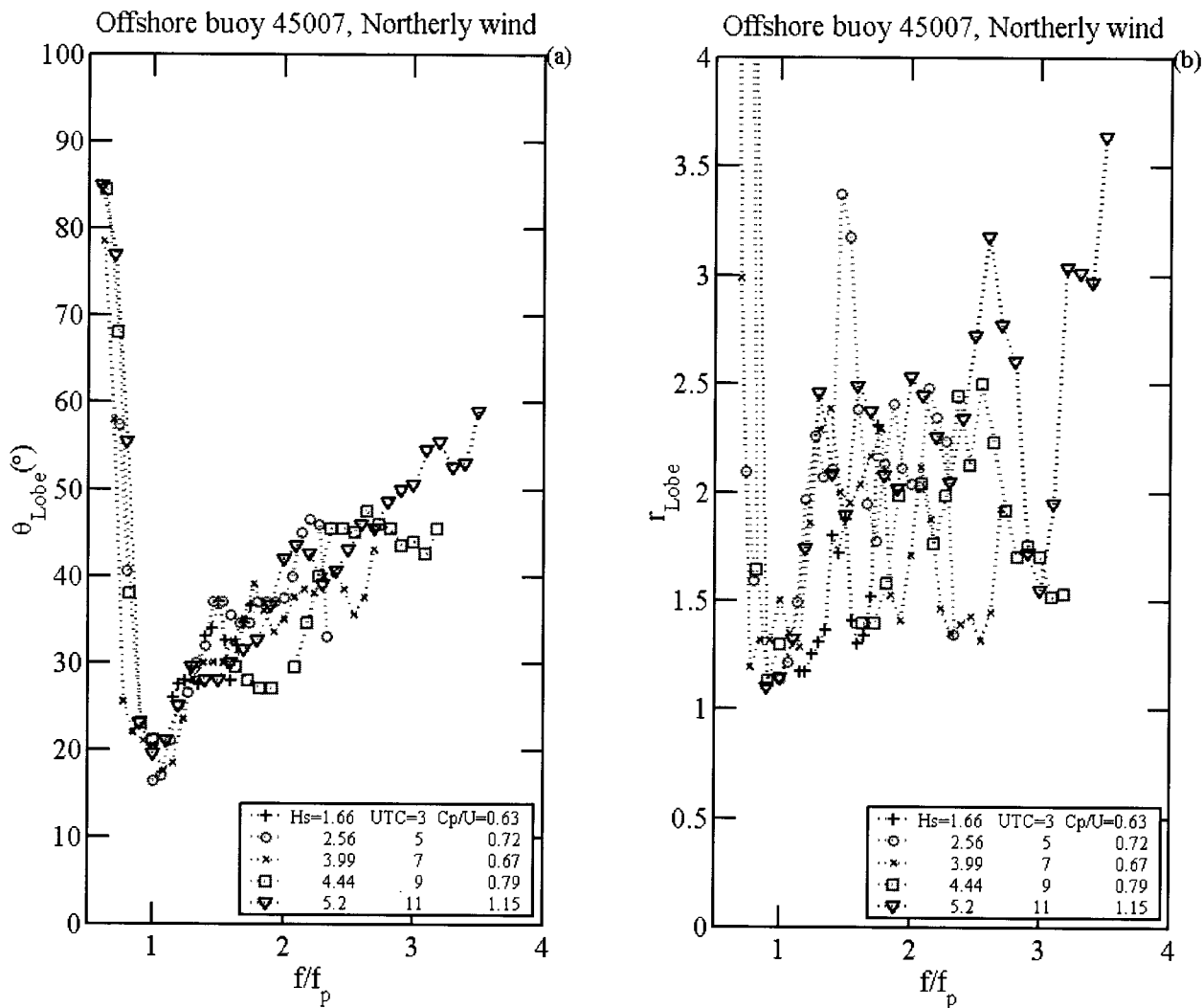


FIG. 14. (a) Lobe separation angle θ_{Lobe} vs f/f_p and (b) lobe ratio r_{Lobe} vs f/f_p for the directional distributions of the 5th, 7th, 9th, 11th, and the last hours of the northerly event at the offshore buoy.

due to land proximity, and slant fetch effect in wave development.

c. Lobe ratio

Figure 14b shows the plot of r_{Lobe} as a function of f/f_p for the directional distributions at the same hours as those shown in Fig. 14a. In spite of a considerably larger data scatter of r_{Lobe} than that of θ_{Lobe} , there is a distinct trend that the value of r_{Lobe} increases with frequencies moving away from $f/f_p = 1$. There is no clear dependence of r_{Lobe} on the wave age. The larger data scatter of r_{Lobe} in Fig. 14b is due to sampling variability associated with the directional wave data. The sampling variability causes a larger variation to the distribution amplitude (thus affecting the lobe ratio) than to the bimodal angles (lobe separation angle) (Krogstad 1990). Figure 16 shows the bin-averaged lobe ratio, $\langle r_{\text{Lobe}} \rangle$,

versus f/f_p . The dashed curves represent the model results [case Y10UT in Table 1 of Banner and Young (1994), data provided by Young (1999, personal communication)]. The dashed-dotted curves represent the ATM results (Hwang et al. 2000). The dotted curves represent the results of the empirical bimodal Gaussian distribution function proposed by Ewans (1998). All three curves show that r_{Lobe} increases with increasing frequency from $f/f_p = 1$. At $1 < f/f_p < 2$, the model curve is very close to the ATM curve. At $f/f_p \geq 2$, the model curve shows a much slower rate of increase than the ATM curve. The Ewans curve is very similar to the ATM curve but with a larger offset in f/f_p indicating no directional bimodality ($r_{\text{Lobe}} > 1$) until $f/f_p = 2$, which is higher than $f/f_p = 1.3$ for the ATM results.

For the southerly and northerly events at the offshore buoy, $\langle r_{\text{Lobe}} \rangle$ has a local minimum at $f/f_p = 1$ and increases gradually as frequency increases (Figs. 16c and

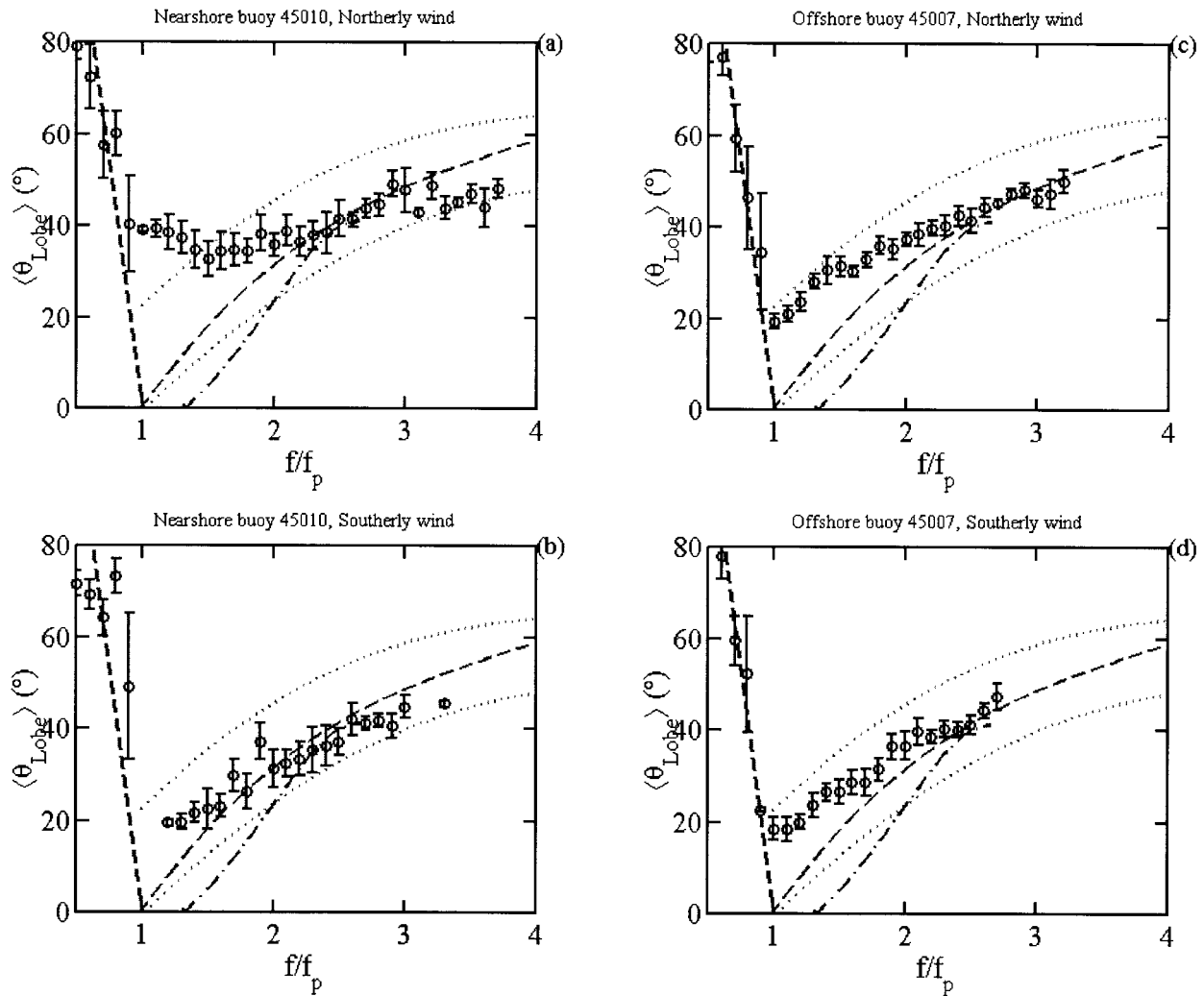


FIG. 15. Bin-averaged separation angle $\langle \theta_{\text{Lobe}} \rangle$ vs f/f_p at the nearshore buoy for (a) the northerly and (b) the southerly events and at the offshore buoy for (c) the northerly and (d) the southerly events. The bin width is $0.2 f/f_p$. The mean value of θ_{Lobe} is marked at the center frequency of each bin as an open circle; the error bar represents one standard deviation. Dashed curve: the model results (Young et al. 1995; Ewans 1998), dashed-dotted curve: the ATM results (Hwang et al. 2000), dotted curves: the upper and lower bounds of the Maui data (Ewans 1998).

16d). This pattern is qualitatively consistent with the results of the model, the ATM, and the Ewans empirical function. At $f/f_p > 2$, $\langle r_{\text{Lobe}} \rangle$ remains much larger than the model curve but closer to the ATM curve. There is a much larger standard deviation in each f/f_p bin at the nearshore buoy (Figs. 16a and 16b) than that at the offshore buoy (Figs. 16c and 16d). This can be in part attributed to the higher sampling variability caused by the lower degree of freedom in the nearshore buoy data but is more likely due to the less homogeneous wind field as a result of land proximity. For the southerly event at the nearshore buoy, $\langle r_{\text{Lobe}} \rangle$ generally increases with increasing frequency from $f/f_p = 1$ (Fig. 16b) and is much larger than that at the offshore buoy (Fig. 16d). For the northerly event at the nearshore buoy, $\langle r_{\text{Lobe}} \rangle$ has a local minimum at about $f/f_p = 2$. As discussed

earlier, the differences of wind and peak wave directions during the northerly event at the nearshore buoy are much larger than those of the southerly event and may present a different condition for the wind wave growth.

d. Asymmetry of bimodal directional distribution

Asymmetric directional distributions are also observed by Young et al. (1995) and Ewans (1998). Young et al. (1995) attributes the asymmetries to the effects of sampling variability. Ewans (1998) postulates that residual effects of low-frequency swell and asymmetry in the wind fetch cause the asymmetries. Asymmetric bimodal distributions are most visible during the two events at the nearshore buoy (Figs. 10c–e, h–j). This observation strongly suggests that inhomogeneous wind

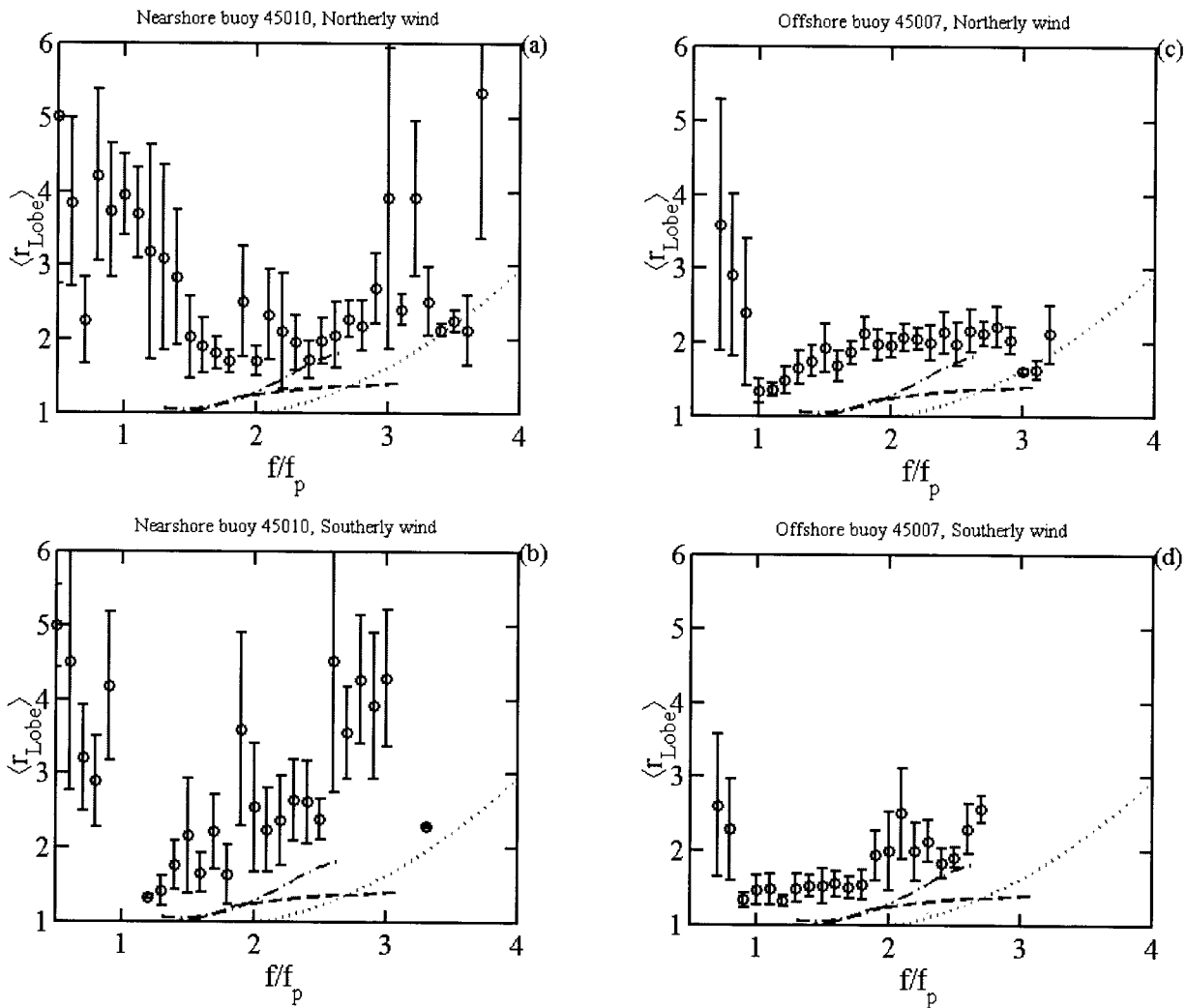


FIG. 16. Bin-averaged lobe ratio $\langle r_{\text{Lobe}} \rangle$ vs f/f_p at the nearshore buoy for (a) the northerly and (b) the southerly events and at the offshore buoy for (c) the northerly and (d) the southerly events. The bin width, symbols, and line styles are the same as those in Fig. 15.

fields due to land proximity, slant fetch effects, and difference in wind and wave directions all could contribute to the asymmetric wave directional distributions. To quantify the asymmetric distributions, the ratio of the two sidelobe peak amplitudes, $R_L = D(f; \alpha_1)/D(f; \alpha_2)$, is computed. A deviation of R_L from unity is an indication of an uneven energy distribution between the two sidelobes. Another parameter that can be used to quantify the asymmetry is the skewness γ of the distribution function, defined as (Kuik et al. 1988)

$$\gamma = \frac{\mu_3}{\sigma^2}, \quad (12)$$

where σ , defined as

$$\sigma = \mu_2^{1/2}, \quad (13)$$

is equivalent to the root-mean-square angular deviation (Longuet-Higgins et al. 1963), and

$$\mu_n = \int_{\theta_m - \pi}^{\theta_m + \pi} (\theta - \theta_m)^n D(f, \theta) d\theta \quad (14)$$

is the n th moment centered at mean direction θ_m , defined as

$$\theta_m = \int_{-\pi}^{\pi} \theta D(f, \theta) d\theta. \quad (15)$$

For a perfectly symmetric distribution with respect to θ_m , the skewness is zero. The skewness can be positive or negative depending on the location of the mode of distribution with respect to θ_m .

Figure 17 shows the bin-averaged $\langle R_L \rangle$ versus f/f_p . For the two events at the offshore buoy site where the effect of an inhomogeneous wind field due to land proximity is not expected, the directional distributions are generally symmetric (see Fig. 7). Most $\langle R_L \rangle$ varies

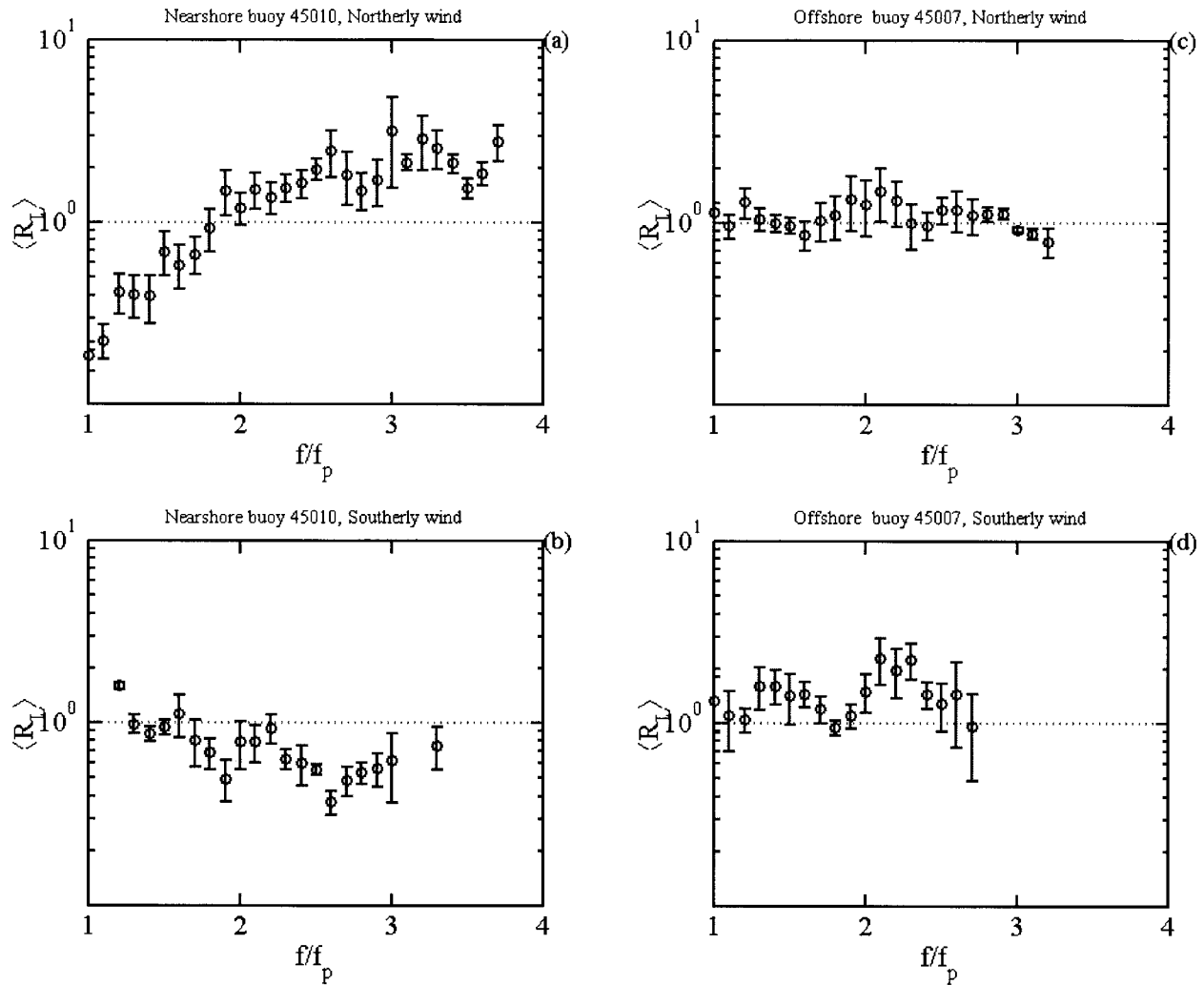


FIG. 17. Bin-averaged ratio of the sidelobe peak amplitudes $\langle R_L \rangle$ vs f/f_p at the nearshore buoy for (a) the northerly and (b) the southerly events and at the offshore buoy for (c) the northerly and (d) the southerly events. The dotted lines indicate $\langle R_L \rangle = 1$ for symmetric directional distribution. The bin width and symbols are the same as those in Fig. 15.

around unity in the range from 0.8 to 1.6 with no clear systematic dependence on f/f_p (Figs. 17c and 17d). Ewans (1998, Fig. 13) reports that most R_L are substantially less than 1 at $f/f_p < 1.3$ and are only slightly different from unity at $f/f_p \geq 1.3$.

For the two events at the nearshore buoy (Figs. 17a and 17b), $\langle R_L \rangle$ shows a frequency dependence trend at $f/f_p < 2.5$. The dependence is more prominent for the northerly event than the southerly event, which is due to wind waves of the northerly event being more fully developed as a result of the longer wind fetch; $\langle R_L \rangle$ of the northerly event has a lowest value about 0.2 at $f/f_p = 1$ and increases as frequency increases. The $\langle R_L \rangle$ exceeds 1 at $f/f_p = 1.8$ and increases to 2 at $f/f_p = 2.5$. At $f/f_p > 2.5$, $\langle R_L \rangle$ vary in the range from 1.5 to 3 with no dependence on f/f_p . Figure 18 shows the bin-averaged skewness $\langle \gamma \rangle$ versus f/f_p for the two events at the

nearshore (Figs. 18a and 18b) and the offshore buoys (Figs. 18c and 18d). The frequency dependence of $\langle \gamma \rangle$ is very similar to that of $\langle R_L \rangle$ shown in Fig. 17.

For the northerly event at the nearshore buoy (Figs. 17a and 18a), the asymmetry of the directional distribution is closely associated with two factors: 1) the inhomogeneous wind field due to land proximity and 2) the difference between wind and peak wave directions; the range is from 40° to 60° as the wind shifts to more northwesterly and the peak wave direction shifts to more easterly. In the frequency range $1 \leq f/f_p \leq 1.8$, $\langle R_L \rangle$ and $\langle \gamma \rangle$ are, respectively, less than 1 and 0 indicating that there is more wave energy distributed in the sidelobe closer to the northeasterly peak wave direction. At $f/f_p > 1.8$, $\langle R_L \rangle$ and $\langle \gamma \rangle$ exceed, respectively, 1 and 0 indicating that the asymmetry of the directional distribution is reversed and more wave energy is distributed

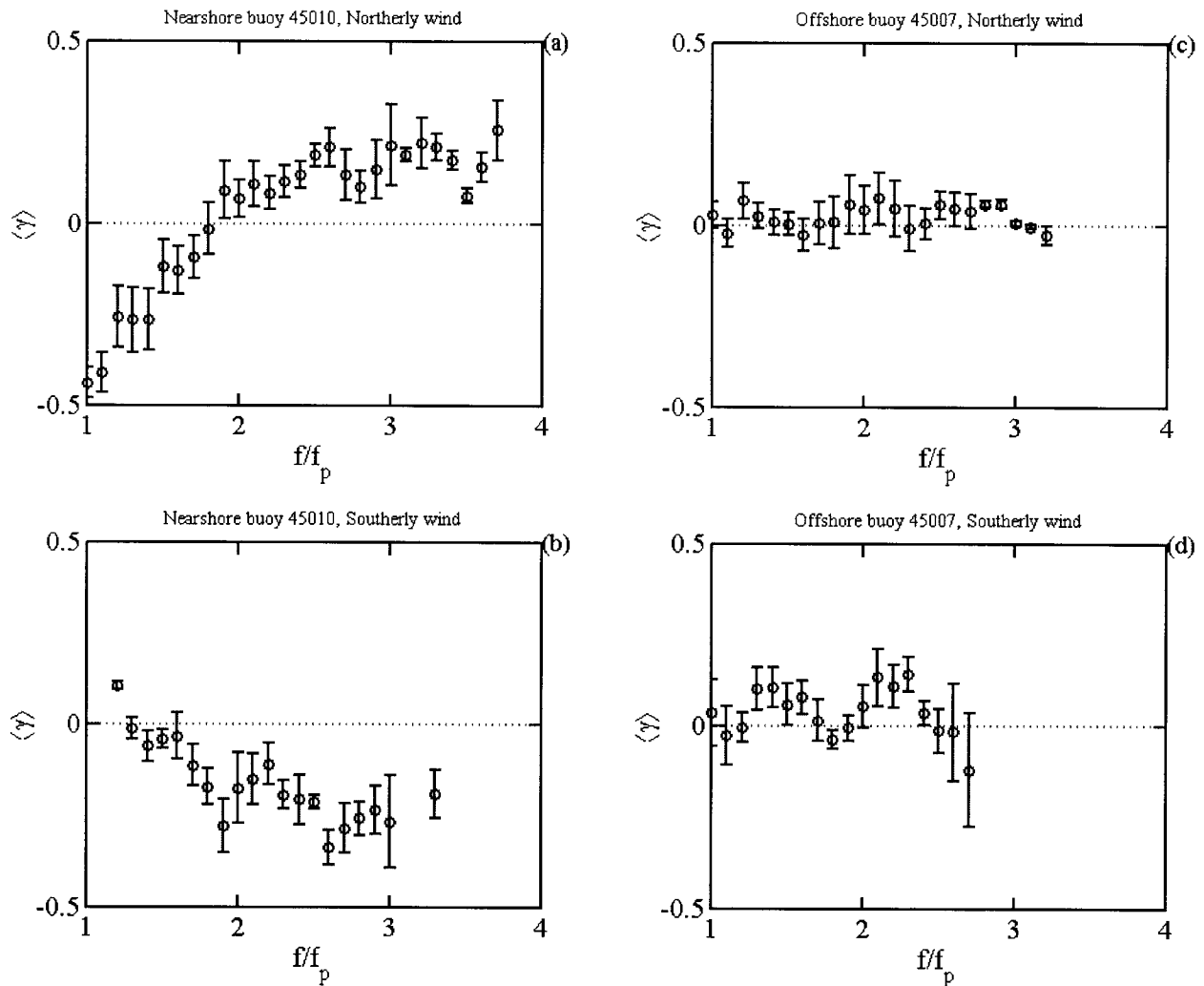


FIG. 18. Bin-averaged skewness $\langle \gamma \rangle$ vs f/f_p at the nearshore buoy for (a) the northerly and (b) the southerly events and at the offshore buoy for (c) the northerly and (d) the southerly events. The dotted lines indicate $\langle \gamma \rangle = 0$ for symmetric directional distribution. The bin width and symbols are the same as those in Fig. 15.

in the sidelobe closer to the northwesterly wind direction.

For the southerly event, the difference of wind and peak wave directions is small. Most $\langle R_L \rangle$ and $\langle \gamma \rangle$ remain less than 1 and 0, respectively, which indicate that more wave energy is distributed in the sidelobe in the offshore propagating direction (Figs. 11e,i,j). This is counterintuitive, as the effect of inhomogeneous wind field due to land proximity will predict the opposite. It is noted that the wind direction is undergoing a continuous shift starting from the offshore direction prior to and at the beginning of the southerly event. The asymmetry in the high-frequency range ($f/f_p > 1.8$) exists throughout the 9-h growth period analyzed in this study. In their research of very small ocean waves (capillary-gravity and short gravity waves wavelengths from 4 mm to 10 cm), Hwang et al. (1996) noticed many significant differences

in the properties of wave spectra obtained from the ocean environments and various laboratory facilities. After examining several possibilities, including surface conditions (active film contamination), fetch differences, and the disparity in the dominant wave conditions, they suggest that small-scale fluctuations in the wind field are probably the largest factors affecting the properties of very small-scale waves. The observations from the nearshore buoy data appear to indicate that the effect of small-scale fluctuation reaches to a much broader band of wave components, with say less than 3-s wave periods. More quantitative investigation of the wind fluctuation aspect is in progress.

The skewness γ is an integrated parameter of the bimodal distribution (12). In contrast, R_L is computed based on the two sidelobe amplitudes of the bimodal distribution. Despite the difference of their derivations,

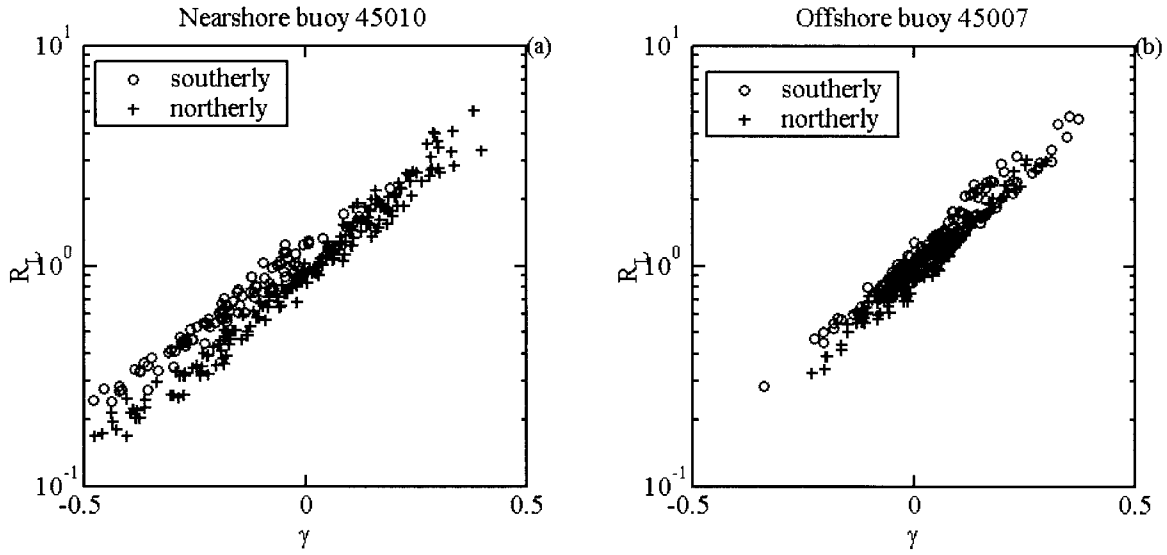


FIG. 19. Skewness γ vs R_L for the directional distributions at (a) the nearshore and (b) the offshore buoys. The data of the southerly and the northerly events are marked as (\circ) and ($+$), respectively.

R_L and γ are closely related (Fig. 19). Computationally, γ is much simpler to obtain.

5. Summary

In this study, a comprehensive analysis is carried out on the wave directional distributions during two active wave growth periods at two buoy stations in Lake Michigan. The directional distribution from buoy temporal measurements is estimated by an empirical method (EMP) averaging the estimates of MLM and MEM. Compared with directional distributions from high-resolution 3D spatial topography of ocean surface waves measured by an airborne scanning lidar system, the EMP estimate is shown to produce a better agreement than the estimates by the MLM and MEM. In this paper, a numerical simulation is performed to compare the bimodal resolution of the three methods. The results fur-

ther confirm that the EMP outperforms the MLM and MEM.

The analysis shows that the bimodal directional distribution is a distinctive and persistent feature over a broad frequency range throughout the wave growing process. The characteristics of directional bimodality can be quantified by the parameters of lobe separation angle θ_{Lobe} and lobe ratio r_{Lobe} . Both parameters show dependencies on the normalized frequency f/f_p with a local minimum at the peak frequency and the magnitude increases monotonically as the wave frequency increases or decreases. These frequency dependencies of the bimodal parameters during the transient wave growth period are consistent with the results under steady wind conditions from reported field studies (Ewans 1998; Hwang et al. 2000) and nonlinear model simulations (Banner and Young 1994). This consistency suggests that directional bimodality is a very robust feature occurring even in waves generated by unsteady wind (growing wind) in both deep and shallow waters. The frequency dependencies of the bimodal parameters are found to be invariant with respect to the wave age during the transient wave growth period. At the offshore buoy where local wind and peak wave directions align closely, the bimodal distributions are symmetric about the wind direction. At the nearshore buoy where the peak wave direction is not in the local wind direction, possibly due to the slant fetch effect of the shoreline orientation and the less homogeneous and more fluctuating wind field, the bimodal distribution is much more asymmetric. The asymmetry can be quantified equally well by the ratio of the two sidelobe amplitudes or the skewness of the bimodal directional distribution. The later of the two parameters is much easier to calculate. Many of the abnormalities of the bimodal distributions at the near-

TABLE 1. Mean and standard deviation (std dev) of the weighted average percent error of the five simulation comparisons ($\beta = 0.02, 0.03, 0.04, 0.05, \text{ and } 0.06$) at different wavenumbers.

k/k_p	WAPE (%)		
	MLM	MEM	EMP
	mean/(std dev)	mean/(std dev)	mean/(std dev)
1	33/(2.3)	28/(10.5)	28 /(4.7)
2	23/(2.3)	25/(11.3)	22 /(5.9)
3	18 /(2.2)	23/(11.5)	18 /(5.7)
4	18/(1.6)	21/(11.2)	15 /(5.2)
5	18/(1.1)	20/(10.6)	14 /(4.6)
6	19/(0.6)	19/(10.2)	13 /(4.0)
7	20/(0.6)	18/(9.8)	12 /(3.5)
8	22/(0.5)	19/(9.3)	12 /(3.1)
9	25/(0.4)	19/(9.5)	13 /(2.8)
10	30/(0.3)	21/(10.1)	15 /(2.1)

TABLE 2. Statistics of hourly wind and wave measurements at the two buoy stations.

Station (ID) events	Offshore buoy (45007)		Nearshore buoy (45010)	
	Southerly	Northerly	Southerly	Northerly
Starting time (UTC/day)	1500/9	2300/10	1400/9	2100/10
Duration (h)	11	13	9	14
Max wind speed (m s^{-1})	15.7	18.0	15.1	16.4
Max significant wave height, H_s (m)	3.64	5.20	2.52	3.28
Max peak period, T_p (s)	7.7	10	7.7	8.3
Wave age	0.60–0.87	0.63–1.15	0.58–0.7	0.58–1.12
Avg wind direction/(std dev) ($^\circ$)	168/(12)	2/(12)	163/(12)	351/(11)
Avg peak wave direction/(std dev) ($^\circ$)	186/(11)	350/(9)	150/(10)	33/(16)

shore buoy of the southerly event in the high-frequency range ($f/f_p > 1.8$), such as the larger lobe ratio and high asymmetry, may indicate that small-scale fluctuations of wind field play an important role in the properties of short waves, consistent with the observations of very small-scale waves (Hwang et al. 1996).

Acknowledgments. This work is sponsored by the Office of Naval Research through the Naval Research Laboratory's research project Phase-Resolved Nonlinear Transformation of Shoaling Waves (Program Element 62435N). The in situ wind and wave data were supplied by the National Data Buoy Center, National Oceanographic and Atmospheric Administration. The nearshore buoy was supported by the Great Lake Environmental Laboratory Nearshore Hydrodynamics Program. We are grateful to the two anonymous reviewers who provided many constructive comments and suggested the simulation test presented in section 2b.

REFERENCES

- Banner, M. L., and I. R. Young, 1994: Modeling spectral dissipation in the evolution of wind waves. Part I: Assessment of existing model performance. *J. Phys. Oceanogr.*, **24**, 1550–1571.
- Benoit, M., 1992: Practical comparative performance survey of methods used for estimating directional wave spectra from heave-pitch-roll data. *Proc. 23d Int. Conf. on Coastal Engineering*, Vol. 2, Venice, Italy, American Society of Civil Engineers, 162–75.
- , P. Frigaard, and H. A. Schaffer, 1997: Analyzing multidirectional wave spectra: A tentative classification of available methods. *Proc. IAHR Seminar on Multidirectional Waves and Their Interaction with Structures*, San Francisco, CA, International Assembly of Hydraulic Research, 131–158.
- Brissette, F. P., and J. Wu, 1992: Wave directional spectra and current interaction in Lake St. Clair. *Proc. Third Int. Workshop on Wave Hindcasting and Forecasting*, Montreal, PQ, Canada, Environment Canada, 24–31.
- , and I. K. Tsanis, 1994: Estimation of wave directional spectra from pitch-roll buoy data. *J. Waterway, Port, Coastal Ocean Eng.*, **120**, 93–115.
- Cote, L. J., and Coauthors, 1960: The directional spectrum of a wind generated sea as determined from data obtained by the Stereo Wave Observation Project. *Meteor. Papers*, Vol. 2, New York University, 88 pp.
- Donelan, M. A., J. Hamilton, and W. H. Hui, 1985: Directional spectra of wind-generated waves. *Philos. Trans. Roy. Soc. London*, **A315**, 509–562.
- Earle, M. D., 1996: Nondirectional and directional wave data analysis procedures. NDBC Tech. Doc. 96-01, National Data Buoy Center, 35 pp.
- Ewans, K. C., 1998: Observations of the directional spectrum of fetch-limited waves. *J. Phys. Oceanogr.*, **28**, 495–512.
- , and T. Van der Vlugt, 1999: Estimating bimodal frequency-direction spectra from surface buoy data recorded during tropical cyclones. *J. Offshore Mech. Arctic Eng.*, **121**, 172–180.
- Gilhousen, D. B., 1987: A field evaluation of NDBC moored buoy winds. *J. Atmos. Oceanic Technol.*, **4**, 94–104.
- , 1989: Field evaluation of NDBC directional wave data. *Proc. Second Int. Workshop on Wave Hindcasting and Forecasting*, Vancouver, BC, Canada, Environment Canada, 1–10.
- Hasselmann, D. E., M. Dunkel, and J. A. Ewing, 1980: Directional wave spectra observed during JONSWAP 1973. *J. Phys. Oceanogr.*, **10**, 1264–1280.
- Hasselmann, K., 1962: On the non-linear energy transfer in a gravity-wave spectrum. 1: General theory. *J. Fluid Mech.*, **15**, 273–281.
- Holthuijsen, L. H., 1983: Observations of the directional distribution of ocean-wave energy in fetch-limited conditions. *J. Phys. Oceanogr.*, **13**, 191–207.
- Hwang, P. A., S. Atakturk, M. A. Sletten, and D. B. Trizna, 1996: A study of the wavenumber spectra of short water waves in the ocean. *J. Phys. Oceanogr.*, **26**, 1266–1285.
- , D. W. Wang, E. J. Walsh, W. B. Krabill, and R. N. Swift, 2000: Airborne measurements of the wavenumber spectra of ocean surface waves. Part 2. Directional distribution. *J. Phys. Oceanogr.*, **30**, 2768–2787.
- Jackson, F. C., W. T. Walton, and C. Y. Peng, 1985: A comparison of in situ and airborne radar observations of ocean wave directionality. *J. Geophys. Res.*, **90**, 1005–1018.
- Krogstad, H. E., 1990: Reliability and resolution of directional wave spectra from heave, pitch, and roll data buoys. *Directional Ocean Wave Spectra*, R. C. Beal, Ed., Johns Hopkins University Press, 66–71.
- Kuik, A. J., G. Ph. Van Vledder, and L. H. Holthuisen, 1988: A method for the routine analysis of pitch-and-roll buoy wave data. *J. Phys. Oceanogr.*, **18**, 1020–1034.
- Liu, P., 1997: Nearshore hydrodynamics studies in western Lake Michigan, 1993–1995. NOAA Tech. Memo. ERL GLERL-103, NOAA/ERL, 40 pp.
- Longuet-Higgins, M. S., D. E. Cartwright, and N. D. Smith, 1963: Observations of the directional spectrum of sea waves using the motions of a floating buoy. *Ocean Wave Spectra*, Prentice Hall, 111–136.
- Lygre, A., and H. E. Krogstad, 1986: Maximum entropy estimation of the directional distribution in ocean wave spectra. *J. Phys. Oceanogr.*, **16**, 2052–2060.
- Mitsuyasu, H., and Coauthors, 1975: Observations of the directional spectrum of ocean waves using a cloverleaf buoy. *J. Phys. Oceanogr.*, **5**, 750–760.
- Oltman-Shay, J., and R. T. Guza, 1984: A data-adaptive ocean wave directional spectrum estimator for pitch-roll type measurements. *J. Phys. Oceanogr.*, **14**, 1800–1810.
- Phillips, O. M., 1958: On some properties of the spectrum of wind-generated ocean waves. *J. Mar. Res.*, **16**, 231–240.

- , 1985: Spectral and statistical properties of the equilibrium range in wind-generated gravity waves. *J. Fluid Mech.*, **156**, 505–531.
- Steele, K. E., and M. D. Earle, 1991: Directional ocean wave spectra using buoy azimuth, pitch and roll derived from magnetic field components. *J. Oceanic Eng.*, **16**, 427–433.
- , C. C. Teng, and D. W. Wang, 1992: Wave direction measurements using pitch-roll buoys. *Ocean Eng.*, **19**, 349–375.
- Walsh, E. J., D. W. Hancock, D. E. Hines, R. N. Swift, and J. F. Scott, 1989: An observation of the directional wave spectrum evolution from shoreline to fully developed. *J. Phys. Oceanogr.*, **19**, 670–690.
- Wyatt, L. R., 1995: The effect of fetch on the directional spectrum of Celtic Sea storm waves. *J. Phys. Oceanogr.*, **25**, 1550–1559.
- Young, I. R., 1994: On the measurement of directional wave spectra. *Appl. Ocean Res.*, **16**, 283–294.
- , and G. Ph. Van Vledder, 1993: A review of the central role of nonlinear interactions in wind-wave evolution. *Philos. Trans. Roy. Soc. London*, **A342**, 505–524.
- , L. A. Verhagen, and M. L. Banner, 1995: A note on the bimodal directional spreading of fetch-limited wind waves. *J. Geophys. Res.*, **100**, 773–778.